

Anatomy of apparent seasonal variations from GPS-derived site position time series

D. Dong,¹ P. Fang,² Y. Bock,² M. K. Cheng,³ and S. Miyazaki^{4,5}

Received 6 April 2001; revised 2 November 2001; accepted 7 November 2001; published 19 April 2002.

[1] Apparent seasonal site position variations are derived from 4.5 years of global continuous GPS time series and are explored through the “peering” approach. Peering is a way to depict the contributions of the comparatively well-known seasonal sources to garner insight into the relatively poorly known contributors. Contributions from pole tide effects, ocean tide loading, atmospheric loading, nontidal oceanic mass, and groundwater loading are evaluated. Our results show that ~40% of the power of the observed annual vertical variations in site positions can be explained by the joint contribution of these seasonal surface mass redistributions. After removing these seasonal effects from the observations the potential contributions from unmodeled wet troposphere effects, bedrock thermal expansion, errors in phase center variation models, and errors in orbital modeling are also investigated. A scaled sensitivity matrix analysis is proposed to assess the contributions from highly correlated parameters. The effects of employing different analysis strategies are investigated by comparing the solutions from different GPS data analysis centers. Comparison results indicate that current solutions of several analysis centers are able to detect the seasonal signals but that the differences among these solutions are the main cause for residual seasonal effects. Potential implications for modeling seasonal variations in global site positions are explored, in particular, as a way to improve the stability of the terrestrial reference frame on seasonal timescales. *INDEX TERMS*: 1223 Geodesy and Gravity: Ocean/Earth/atmosphere interactions (3339); 1247 Geodesy and Gravity: Terrestrial reference systems; *KEYWORDS*: seasonal variation, GPS, time series

1. Introduction

[2] Site-position time series generated from continuous GPS arrays reveal significant seasonal variations, in particular, with an annual period. Here we use the word “seasonal” to represent both annual and semiannual periods. Such apparent seasonal “deformation” is present in global [vanDam and Herring, 1994; vanDam et al., 1994; Blewitt et al., 2000; MacMillan and Ma, 2000; vanDam et al., 2001; Mangialotti et al., 2001] and regional [Hatanaka et al., 2001] time series for sites on all continents. Although the existence of seasonal signals is well known, their systematic investigation has not been performed for two main reasons. First, it was hard to obtain reliable estimates of seasonal variations at global sites from GPS campaign data owing to poor temporal resolution and inadequate distribution of the reference network. Second, lack of global measurements of several important geophysical processes hampered the meaningful comparison between observed and geophysically inferred seasonal variations. Fortunately, both of these weaknesses have been remedied recently. The multiyear daily time series from global continuous GPS arrays provide the temporal resolution required to estimate seasonal variations of site positions. Furthermore, global atmospheric sur-

face pressure data, nontidal oceanic mass redistribution data from space geodesy, and continental waters (soil moisture, snow, and groundwater) mass redistribution data from simulation models are now available to explore the nature of seasonal variations.

[3] In general, the potential contributors to seasonal variations in site positions can be grouped into three categories. The first category stems from gravitational excitation, mostly from the Sun and Moon. The rotational displacements due to seasonal polar motion, universal time corrected for polar motion (UT1) variations and loading-induced displacements due to solid Earth tides, ocean tides, and atmospheric tides all fall into this category. Pole tide loading also belongs to this category with the spectrum of mostly annual and Chandler wobble periods. The second category of seasonal variations is of thermal origin coupled with hydrodynamics. The loading-induced seasonal deformations from atmospheric pressure, nontidal sea surface fluctuations, and groundwater (both liquid and solid) belong in this category. Also included in this category are the thermal expansion of bedrock beneath the GPS benchmark and wind shear—induced site displacements. The third category contains various errors, which also generate apparent seasonal variations. The seasonal errors from satellite orbital models, atmospheric models, water vapor distribution models, phase center variation models, thermal noise of the antenna, local multipath, and snow cover on the antenna all cause apparent variations in estimated site positions. There is another potential but still hypothetical category: tectonic-induced seasonal deformation due to possible seasonal variations in regional fault slip or regional stress.

[4] The benefits from studying the seasonal terms are twofold: (1) to gain insight into the seasonal deformation field caused by various geophysical and tectonic contributors; and (2) to identify the error spectrum of current GPS analysis on seasonal scales. Investigating unmodeled and mismodeled seasonal errors provides critical information for further improving the accuracy of GPS data analysis. In this paper, we first elaborate procedures to obtain seasonal terms of site positions. Then we investigate the effects of known geophysical

¹Jet Propulsion Laboratory, California Institute of Technology, Pasadena, California, USA.

²Institute of Geophysics and Planetary Physics, Scripps Institution of Oceanography, La Jolla, California, USA.

³Center for Space Research, University of Texas at Austin, Austin, Texas, USA.

⁴Geodetic Observation Center, Geographical Survey Institute, Ibaraki, Japan.

⁵Now at Earthquake Research Institute, University of Tokyo, Tokyo, Japan.

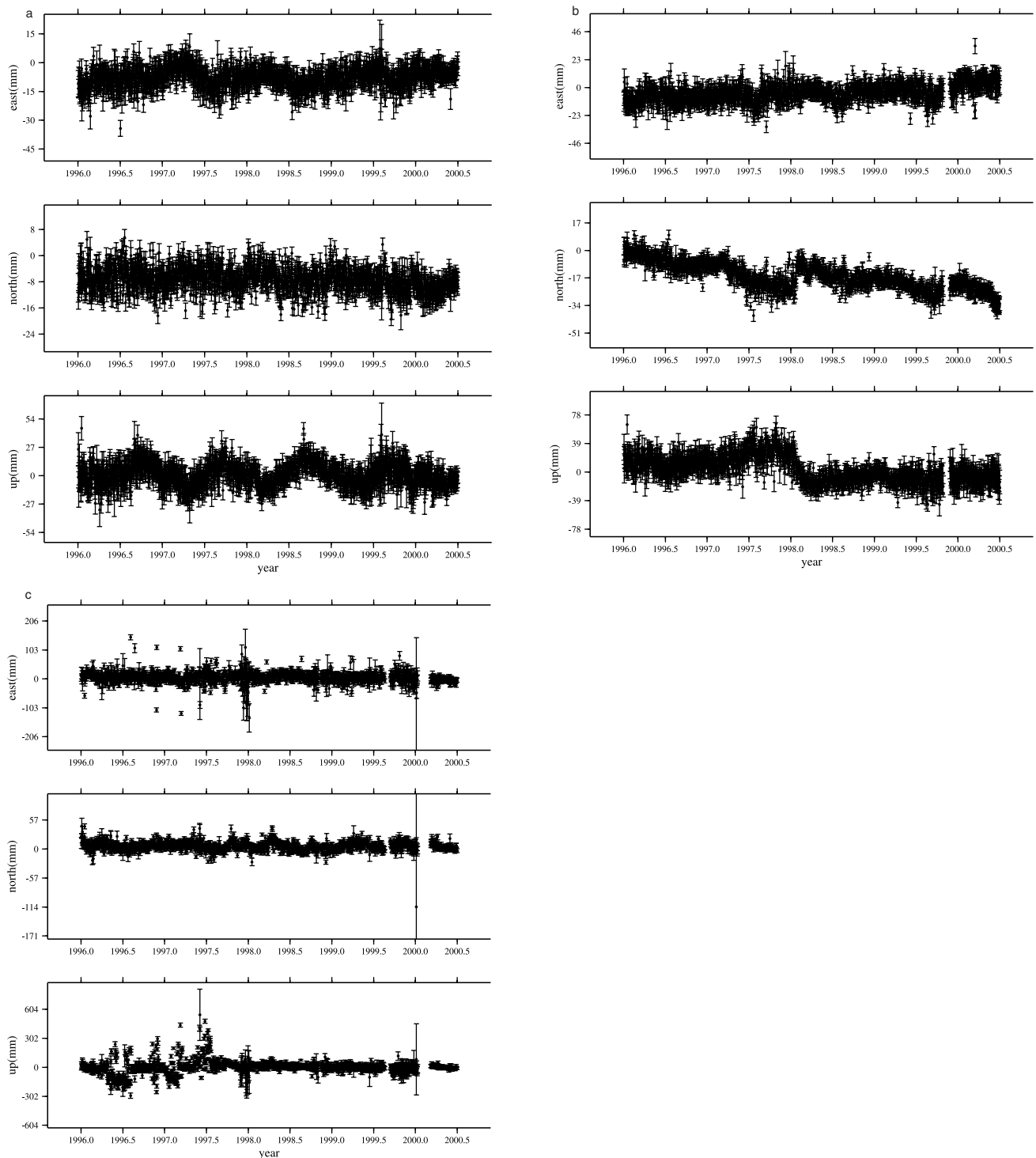


Figure 1. Detrended time series of coordinate adjustments at sites (a) ALBH, (b) HOLP, and (c) KOUR. On 23 January 1998 of the HOLP time series, there were jumps (due to trimming tree) of -0.3 , 10.2 , and -36.8 mm for east, north, and up components, respectively. On 16 October 1999 of the HOLP series, there were jumps (due to the Hector Mine earthquake) of 4.0 , 4.5 , and -6.2 mm for east, north, and up components, respectively.

sources and potential contributors. Finally, we discuss the importance of understanding seasonal variations in site positions.

2. Time Series Analysis

[5] We examine the continuous GPS array daily solutions generated at the Scripps Orbit and Permanent Array Center

(SOPAC) (available at <http://sopac.ucsd.edu>) in the 4.5-year period from January 1996 to June 2000. The daily GPS observation data from the global network (totaling 429 sites) were processed using the GAMIT software [King and Bock, 2000]. To reduce the computational burden and to keep solutions consistent with the global network analysis, the cluster analysis technique [Blewitt *et al.*, 1993] was adopted. The 429 sites were distributed into five subnet-

Table 1. Global GPS Sites

Site	Longitude	Latitude	Site	Longitude	Latitude	Site	Longitude	Latitude
ALBH ^a	236.513	48.390	HOFN	344.802	64.267	PIN1	243.542	33.612
ALGO ^a	281.929	45.956	HVLK	260.893	37.651	PLTC	255.274	40.182
ANKR	32.758	39.887	IISC	77.570	13.021	POL2	74.694	42.680
AOA1	241.170	34.157	IRKT	104.316	52.219	POTS ^a	13.066	52.379
AOML	279.838	25.735	JOZE	21.032	52.097	PRCO	262.481	34.980
AREQ	288.507	-16.466	JPLM	241.827	34.205	PRDS	245.707	50.871
ASC1	345.588	-7.951	KATZ	35.688	32.995	PVEP	241.596	33.743
AUCK	174.834	-36.603	KELY	309.055	66.987	QUIN	239.056	39.975
BAHR	50.608	26.209	KERG ^a	70.256	-49.351	REYK ^a	338.045	64.139
BOGT	285.919	4.640	KIRU	20.968	67.857	SANT	289.331	-33.150
BOR1	17.073	52.277	KIT3	66.885	39.135	SCH2	293.167	54.832
BRAZ	312.122	-15.947	KOKB ^a	200.335	22.126	SELE	77.017	43.179
BRMU ^a	295.304	32.370	KOSG ^a	5.810	52.178	SHAO ^a	121.200	31.100
BRUS	4.359	50.798	KOUR	307.194	5.252	STJO ^a	307.322	47.595
CAGL	8.973	39.136	KSTU	92.794	55.993	STRL	282.516	38.977
CARR	239.569	35.888	KWJ1 ^a	167.730	8.722	TAEJ	127.366	36.374
CASI	110.520	-66.283	LHAS	91.104	29.657	TAHI	210.391	-17.577
CHAT	183.434	-43.956	LMNO	262.519	32.668	TEL ^a	34.781	32.068
CHUR	265.911	58.759	LPGS	302.068	-34.907	THU1	291.212	76.537
CICE	243.333	31.871	MAC1 ^a	158.936	-54.500	TIBB	237.552	37.891
CIT1	241.873	34.137	MAGO	150.770	59.576	TIDB ^a	148.980	-35.399
COCO	96.834	-12.188	MALI ^a	40.194	-2.996	TMGO	254.767	40.131
CRO1	295.416	17.757	MAS1 ^a	344.367	27.764	TOUL	1.481	43.561
DAV1 ^a	77.973	-68.577	MATE ^a	16.704	40.649	TSKB ^a	140.087	36.106
DGAR	72.370	-7.270	MCM4	166.669	-77.838	UCLP	241.558	34.069
DQUA	265.710	34.111	MDO1 ^a	255.985	30.681	USUD ^a	138.362	36.133
DRAO ^a	240.375	49.323	MDVO	37.224	56.027	VCIO	260.783	36.072
DUBO	264.134	50.259	METS	24.395	60.217	VILL ^a	356.048	40.444
EISL	250.617	-27.148	MKEA	204.544	19.801	VNDP	239.384	34.556
ELAT	34.921	29.509	NOUM	166.410	-22.270	WES2 ^a	288.507	42.613
FAIR ^a	212.501	64.978	NDBC	270.390	30.356	WHIT	224.778	60.751
FLIN	258.022	54.726	NDSK	264.362	37.381	WLPS	284.530	37.937
FORT ^a	321.574	-3.877	NLIB ^a	268.425	41.772	WSMN	253.650	32.407
GDAC	257.820	37.775	NOTO	14.990	36.876	WSRT	6.605	52.915
GOLD ^a	243.111	35.425	NRC1	284.376	45.454	WTZR ^a	12.879	49.144
GOPE	14.786	49.914	NTUS	103.680	1.346	XIAN	109.221	34.369
GRAS	6.921	43.755	NYAL	11.865	78.930	YAKZ	129.681	62.031
GRAZ ^a	15.493	47.067	OBER	11.280	48.086	YAR1 ^a	115.347	-29.047
GUAM ^a	144.868	13.589	OHIG	302.100	-63.321	YELL ^a	245.519	62.481
HARK ^a	27.708	-25.887	ONSA ^a	11.926	57.395	ZECK	41.565	43.788
HBRK	262.706	38.305	PATT	264.281	31.778	ZIMM	7.465	46.877
HKLO	264.137	35.683	PERT ^a	115.885	-31.802	ZWEN	36.759	55.699
HOB2	147.439	-42.805	PIE1 ^a	251.881	34.302			

^a Core site used to construct the network constraint.

works (two International GPS Service (IGS) subnetworks, one in Eurasia, one in California, and one in the central United States). Each subnetwork consists of three to five core sites redundant with the IGS [Beutler *et al.*, 1994] subnetworks. In the primary data analysis, effects of solid Earth tides (including annual and semi-annual tides) were modeled and removed based on Wahr's model and 18.6-year equilibrium tide model. Aside from estimating site coordinates and satellite orbital parameters (six states and nine general radiation parameters), each daily solution includes earth rotation parameters (polar motion, UT1), multiple atmospheric zenith delays and gradients, and phase ambiguity parameters. All estimated parameters were loosely constrained. Since the baseline lengths of the global sites mostly exceed 500 km, it is difficult to resolve all integer-cycle ambiguities. Therefore for the sake of consistency we did not attempt to resolve the ambiguities. The subnetworks for each day were combined using the GLOBK software version 4.10 [Herring, 2000] to form a single, loosely constrained global daily solution [Dong *et al.*, 1998]. For historical reasons this data set was not totally analyzed in a consistent manner. For example, the satellite elevation cutoff angle was originally set as 15°. From day 166 of 1997 the elevation cutoff angle was changed to 7° and restored to 15° on day 115 of 1999. Starting from day 332 of 1999 the elevation cutoff angle was

switched to 10°. There were also several other changes in analysis strategy, as well as several GAMIT software upgrades. Reprocessing the primary data in a consistent manner will definitely improve the quality of time series and is in progress.

[6] The loosely constrained daily solutions were input as quasi-observations to the Quasi-Observation Combination Analysis (QOCA) software (available at <http://gipsy.jpl.nasa.gov/qoca>) to estimate the time series of site positions. We considered two possible strategies to estimate the seasonal terms from the quasi-observations. One is to perform the global network adjustment by estimating the seasonal terms from all quasi-observations simultaneously. The advantage of this approach is that the full covariance matrix is used, hence all correlations are taken into account. Aside from the significant computational burden its primary disadvantage is that any outlier or misfit of one site will affect the estimates of all the other sites. Another approach is to form the time series of each site from the daily solutions and then estimate the seasonal terms site by site from the time series. The advantage of this approach is that it is easier to detect and handle the position outliers (e.g., from instrumental effects) of each time series. Any misfit of one time series (e.g., local nonseasonal variations) will not affect the estimates of the other sites. The weakness of this approach is that the correlation between each time series is neglected. However,

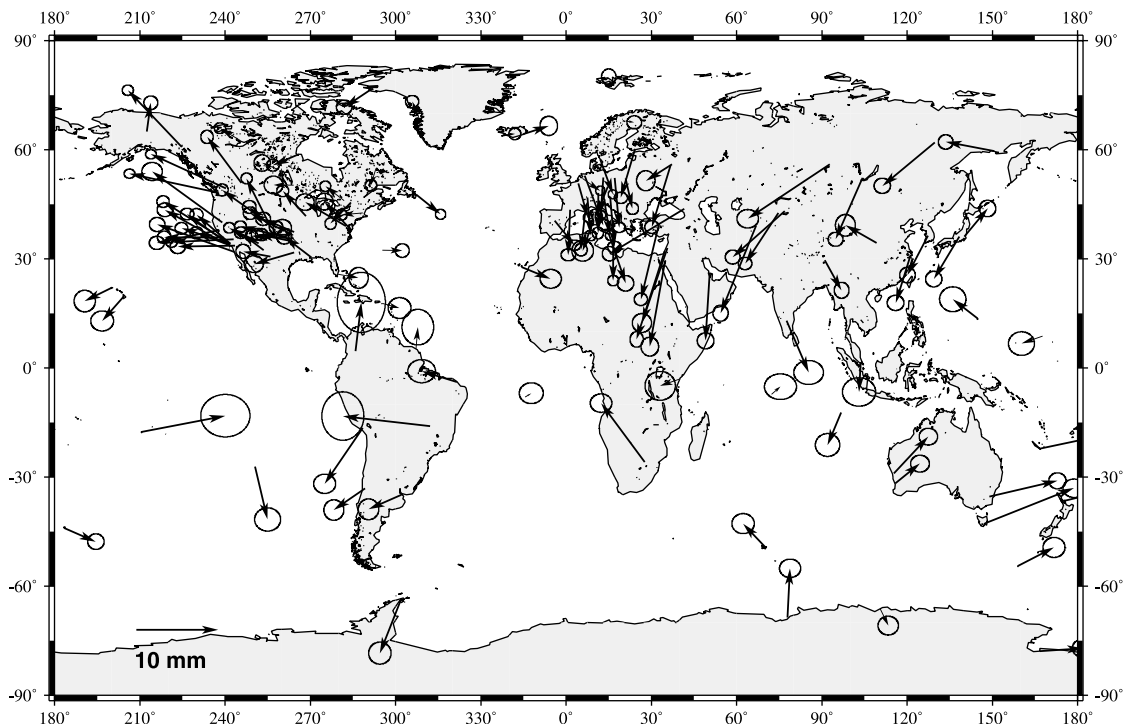


Figure 2. Vertical annual terms of the 128 globally distributed sites. The amplitude A and phase ϕ are defined as $A\sin[\omega(t-t_0) + \phi]$, where t_0 is 1996.0 and ω is the annual angular frequency. The arrows represent the amplitudes. The phases are counted counterclockwise from the east. The ellipses represent the 95% confidence level.

Zhang [1996] showed that these correlations are small. We adopt the second approach because the identification of outliers and misfits are primary considerations (Figure 1 shows three typical time series: ALBH is a normal series, HOLP has one nonseasonal position shift, and KOUR has numerous outliers).

[7] For each daily quasiobservation file the network constraint solution [see Dong *et al.*, 1998, Appendix C] was constructed using 36 globally distributed core sites (Table 1). A seven-parameter transformation (three network rotations, three network translations, and one scaling parameter) was performed, aligning to the International Terrestrial Reference Frame 1997 (ITRF97) no net rotation (NNR) frame [Boucher *et al.*, 1997]. Since the GPS-estimated vertical coordinates usually have poorer accuracy than the horizontal coordinates, we reduced the weight of vertical positions at core sites by a factor of 100 in determining the 7 network parameters. We corrected the time series of core site GOLD for the coseismic displacements induced by the 16 October 1999 Hector Mine earthquake (-5.3 mm east, 0.3 mm north and -2.7 mm vertical based on the analysis of Hurst *et al.* [2000]). The resultant time series have some abnormal outliers so that the scatter clearly does not obey Gaussian statistics. Therefore we used the robust fit algorithm, imbedded in the QOCA software, since it resists outliers better than conventional least squares [Bock *et al.*, 2000]. The formal errors were scaled by the data scatters to reflect more realistic uncertainties.

[8] For each site-position time series we fit a constant bias with respect to epoch 1996.0, a velocity, and amplitudes and phases (sine convention, phase related to 1 January) for annual and semiannual variations for a total of six parameters each for north, east and up components, respectively. In some time series, there are apparent offsets due to antenna changes, modifications in the analysis strategy, and associated model changes. We modeled these offsets as step functions and estimated them together with the above-mentioned six parameters per site coordinate. To get more reliable estimates of the seasonal terms, we did not use sites with observations spanning <2.3 years or with large gaps within the observation

span. This constraint reduced the number of sites from 429 to 171. We also discarded eight sites (such as CASA and HOLP) due to their apparent benchmark instability or site position shifts caused by environmental changes. Four sites (TROM, WUHN, SIO3, and HERS) were not used owing to large scatters from instrumental failure or frequent receiver testing. Furthermore, some sites (HARK/HART, NYAL/NYA1, and TAHI/THI) were shifted to nearby local benchmarks during the 4.5-year period, so we connected their time series by estimating coordinate offsets. We also edited a few time series that showed significant inconsistency between one small segment and the remaining points. We removed the first six months data in 1996 at site KOUR, the entire 1996 data set at site TIDB, data from October 1999 at site GUAM, and the six months data set in 2000 at site ZWEN. Finally, we selected a subset of sites (12 out of 44) with long observation spans from the densely instrumented California region to provide a spatially uniform distribution. This selection process reduced the number of time series from 429 to 128 sites for our analysis of seasonal parameters (Table 1).

[9] Annual vertical variations are found to be most significant in our analysis. Most vertical annual amplitudes are <10 mm, typically $4-10$ mm, while corresponding formal errors are mostly <1 mm. The north and east annual amplitudes are mostly in the range of $1-3$ mm with formal errors of ~ 0.5 mm. The formal errors of the annual phase parameters are typically $5-10^\circ$ for the vertical components and $7-15^\circ$ for the horizontal components.

[10] In this paper, we focus on the vertical components, mainly the annual variation, and only briefly discuss the horizontal components. For each coordinate component we define the weighted mean of amplitude to characterize the power of the annual and semiannual terms. The reason for choosing the weighted mean amplitude instead of power (square of amplitude) is to avoid being overly influenced by a few sites with large seasonal effects. Figure 2 shows the amplitudes and phases of the vertical annual components for the global network. For the 128 sites the weighted mean amplitude of vertical annual terms is 5.47 mm. Although the distributions of the amplitudes and phases are not very regular,

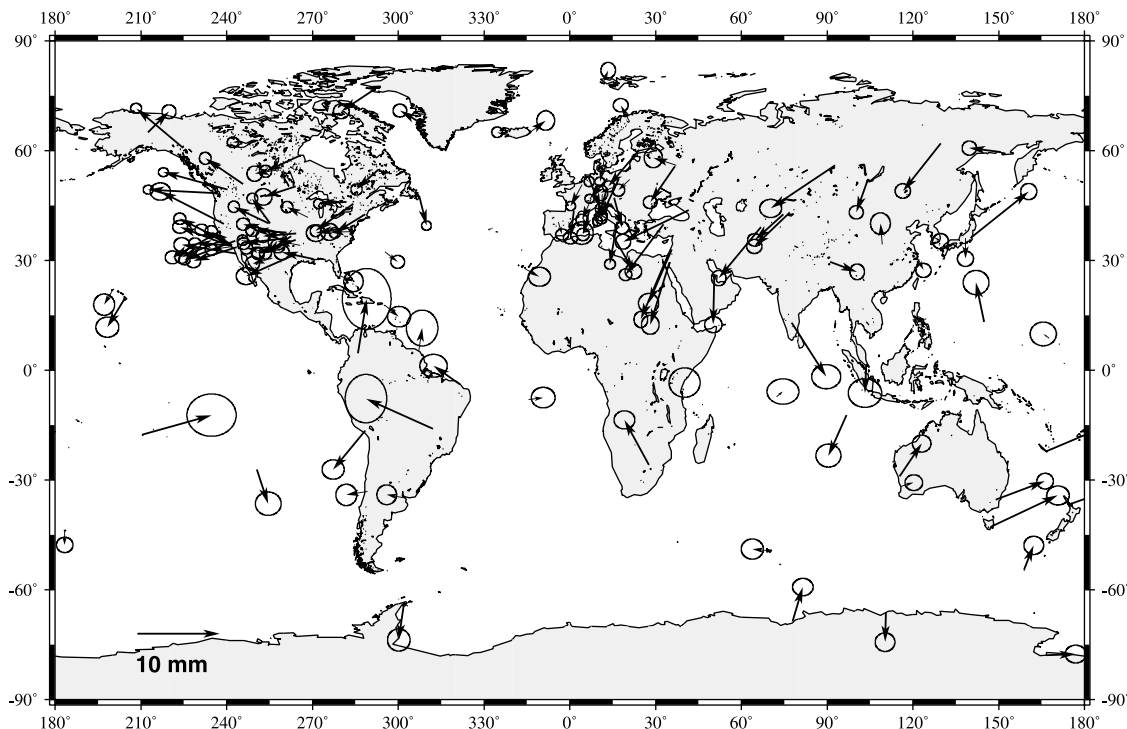


Figure 3. Vertical annual terms (after pole tide and ocean tide corrections). The amplitude and phase are defined the same way as in Figure 2.

they are not randomly distributed either. The sites located in adjacent regions tend to show similar phases. We first check how much amplitude can be explained by the joint contribution of known geophysical causes. Then we explore the causes for residual seasonal effects.

3. Subtracting Seasonal Terms Generated by Known Geophysical Sources

[11] The observed apparent seasonal variations in site positions contain the contributions from various sources. To explore the nature of the observed seasonal variations, an ideal approach is to compare the observed values with the joint contributions from all relevant sources. Such an approach has difficulties because many relevant sources, such as seasonal antenna phase center variations and low-frequency multipath variations, are not well understood. Another approach is to subtract the contributions of the well determined or modeled sources from the observation data first, then study the relation between the observed residual seasonal variations with remaining contributors. We adopt such a “peering” approach. We examine the influence, distribution, and magnitude of individual geophysical sources, which are not modeled in the SOPAC analysis. Since there is no single source playing a dominant role, we compare the joint contribution of these geophysical sources with the observed seasonal variations.

3.1. Pole Tide

[12] The pole tide geometrical correction was imposed using the formulas adopted by the International Earth Rotation Service [McCarthy, 1996]:

$$\begin{aligned} d\lambda &= 9.0 \cos \theta (x_p \sin \lambda + y_p \cos \lambda) \\ d\theta &= -9.0 \cos 2\theta (x_p \cos \lambda - y_p \sin \lambda) \\ dr &= -32.0 \sin 2\theta (x_p \cos \lambda - y_p \sin \lambda), \end{aligned} \quad (1)$$

where x_p, y_p are pole positions in arc seconds, λ is site longitude, θ is site colatitude, and $d\lambda, d\theta$, and dr are the pole tide corrections in millimeters (positive east, south, and upward, subtracted from the site coordinate estimates). The pole positions can reach, at most, 0.8 arc seconds, corresponding to a maximum vertical correction of ~ 25 mm and a maximum horizontal correction of ~ 7 mm. The largest component of the polar motion is the Chandler wobble. The next largest is the annual polar motion with an amplitude of ~ 0.1 arc seconds, corresponding to a maximum vertical annual amplitude correction of ~ 4 mm and a maximum horizontal annual amplitude correction of ~ 1 mm. Figure 3 shows the vertical annual terms after the pole tide correction. Compared with Figure 2, relatively large changes occur for the sites at midlatitudes, in which most annual variations were reduced; in particular, in Eurasia. The weighted mean amplitude of vertical annual terms is reduced from 5.44 to 4.19 mm. At 101 out of 128 sites the vertical annual amplitudes are reduced, as seen by comparing Figure 2 with Figure 3. Meanwhile, at 96 out of 128 sites and at 83 out of 128 sites the eastern and northern annual amplitudes are also reduced. After the pole tide correction the vertical annual amplitudes at most sites < 7 mm.

3.2. Ocean Tide

[13] The ocean tide loading corrections were performed using the coefficients from Scherneck [1991]. These include amplitudes and phases of 11 tides (M2, S2, N2, K2, K1, O1, P1, Q1, MF, MM, and SSA) for each site. For the daily (mean solar day) quasi-observations, if the primary observations were uniformly distributed within 1 day, the effects of semidiurnal and diurnal tides are mostly averaged out. Only a small part remains due to small differences between the tide frequencies and the frequency of mean solar day. Such a small frequency difference related period is called an alias period. The alias periods of K1 and P1 tides are annual. Since we do not have the information of primary observation distribution, it is difficult to assess the aliasing effects in the daily averaged quasi-observations, and we ignore them in this paper. Here we only apply corrections for semimonthly, monthly and

semiannual tides (MF, MM, and SSA). Ocean loading mostly affects the vertical positions. At semiannual periods the typical amplitudes of the vertical position corrections due to ocean tide loading are 1 mm or less. Scherneck's coefficients do not include the annual tide (SA). Since the amplitude of the SA tide potential is only 16% of the amplitude of SSA tide potential, the contribution of the SA tide to vertical coordinates is at the submillimeter level and we ignore it here. Thus the annual terms are virtually unchanged after the ocean tide loading correction.

3.3. Atmospheric Mass Loading

[14] The Green's function approach is adopted to calculate the site displacements from various mass loads such as atmospheric loading [Farrell, 1972; vanDam and Wahr, 1987]. The 6-hour sampling National Center for Environmental Prediction (NCEP) reanalysis surface pressure data from 1996 to 2000 are used to calculate the displacements at each site. Since the quasi-observations used in this work are daily solutions, we use the daily averaged surface pressure data to calculate the corresponding site displacements. The inverted barometer (IB) model is implemented to account for the oceanic response to surface pressure variations, and the European Center for Medium-range Weather Forecasts (ECMWF) land-ocean mask model is utilized. The IB model considers the ocean's response to surface loading as an inverted barometer so that only the mean atmospheric pressure over the world's oceans, rather than the local pressure, is transmitted to the ocean bottom. On seasonal timescales the IB model is generally believed to be a good approximation [Dickman, 1988; Fu and Pihos, 1994]. The vertical coordinate is the component most affected by atmospheric loading. The general pattern is that the amplitudes of seasonal variations of GPS sites on oceanic islands are smaller than within the continents. The largest annual amplitudes from atmospheric loading exceed 4 mm at the sites in the interior of the Eurasian plate and the Arabian Peninsula such as BHR, KSTU, SHAO, and KIT3. The annual amplitudes of horizontal components are generally <0.5 mm. Semiannual vertical amplitudes at most GPS sites are <1 mm. However, sites on the eastern Antarctica coast (DAV1, CAS1, and MCM4) have strong semiannual variations from atmospheric loading with amplitudes of 1.4, 1.7, and 1.8 mm, respectively. There are two approaches to correcting for atmospheric loading. The first is to subtract the calculated daily site displacements caused by atmospheric loading from the daily quasi-observations. This approach removes both high- and low-frequency variations due to atmospheric loading. However, the noise of the atmospheric series also enters into the residual series. The second approach is to adjust the seasonal terms from both the quasiobservation series and the atmosphere-caused site displacement series. Then seasonal terms of the atmosphere-caused displacement series are subtracted from the seasonal terms of the quasiobservation series. This approach is equivalent to the correction from the smoothed atmospheric series. However, the atmosphere caused high-frequency site displacements, and inter-annual site displacements will remain in the residual series. We adopt the first approach because it removes the effects of atmospheric loading at all frequency bands.

3.4. Nontidal Ocean Mass Loading

[15] The nontidal ocean mass migration arises from the interaction of the surface wind driving force, atmospheric pressure, heat and moisture exchange, and hydrodynamics. TOPEX/Poseidon altimeter data measure the time-varying ocean topography with $1^\circ \times 1^\circ$ spatial resolution and 10-day temporal resolution [Tapley et al., 1994]. The altimeter-measured sea surface variations stem from surface barometric pressure change, water mass exchange between ocean, atmosphere, and groundwater, and the wind-forced upwelling/downwelling in the thermocline, referred to as Ekman pumping. Sea surface topography changes caused by atmospheric pressure loading were corrected by the standard IB correction model.

[16] The seasonal steric variations in sea surface, arising from the salinity and temperature variations above the thermocline, do not contribute to the mass variation in the oceans and should be corrected. This dynamic height correction can be calculated in terms of the specific volume anomaly [Gill, 1982] using the World Ocean Atlas (WOA) [Levitus and Boyer, 1994]. The WOA-94 model was used in this study. This model provides monthly averaged fields of temperature and salinity at 19 depths over the global ocean based on historical in situ oceanographic observations. This model shows that the significant seasonal variations of the steric height occur within the upper mixed layer of ocean, in particular, at depths of 50–75 m. The amplitude can be 3.2 cm over the range of latitudes -40° to -30° and longitude 30° to 40° , and the largest amplitude variation of order 4 cm is found at 10 m depth from June to July in the 70° to 80° latitude range [Cheng and Tapley, 1999]. After the corrections we used TOPEX/Poseidon data to infer site coordinate variation time series on the basis of the Green function approach. Before 1997 the inferred site coordinate time series show clear seasonal variations due to nontidal ocean mass loading. From 1997 to 1999, however, the major patterns became interannual due to the strong 1997–1998 El Niño event and the following 1999 La Niña event [McPhaden, 1998]. In particular, El Niño/La Niña-related patterns are most significant for the GPS sites on equatorial islands and coastal regions. Unfortunately, the TOPEX/Poseidon solutions are at 10-day intervals, so that we cannot perform daily corrections for the nontidal oceanic mass induced site displacements. We adjust the seasonal terms of coordinates caused by nontidal oceanic mass redistribution for each site using 1996–2000 TOPEX/Poseidon data solutions. Then we subtract the nontidal oceanic mass caused seasonal terms from the GPS-observed seasonal terms of site coordinates. The largest vertical annual amplitudes reach 2–3 mm at the low-latitude islands and coastal sites. Vertical annual amplitudes at most continental sites are ~ 1 mm or less. Since the TOPEX/Poseidon altimeter data only cover the region between 66°S and 66°N , variations at Antarctica sites and other polar region sites may be underestimated.

3.5. Snow and Soil Moisture Mass Loading

[17] A reliable global climatology model is not available yet for current analysis. Mass redistribution from variations of snow cover and soil moisture is derived from the assimilated model of NCEP/Department of Energy (DOE) Atmospheric Model Intercomparison Project (AMIP)-II Reanalysis (Reanalysis-2) [Kanamitsu et al., 1999; Roads et al., 1999]. The NCEP/DOE AMIP-II Reanalysis-2 is based on the widely used NCEP/National Center for Atmospheric Research (NCAR) Climate Data Assimilation System-1 (CDAS-1) Reanalysis and on attempts to improve the analysis by fixing the known errors and by updating the parameterizations of physical processes. In general, temperatures are assimilated except for over water, where the sea surface temperature and ship temperatures are used. Climate Prediction Center Merged Analysis of Precipitation (CMAP) pentad precipitation data are used to adjust the soil moisture. Comparison with the soil moisture measurements at Illinois State indicates that this model provides better agreement. (see <http://wesley.wvb.noaa.gov/reanalysis2/kana/rean12-1.htm> for details). The soil moisture from this model represents the net water mass stored over the continental areas and islands from a water cycle (precipitation, evaporation, and runoff). Thus the water mass changes in the atmosphere and in the oceans can be computed separately. The spatial resolution of this model is given on a Gaussian grid of 1.875° spacing in longitude and uneven spacing in latitude (94 latitude bands with an average span of 1.904°). The temporal resolution of this model is a month. The monthly mean soil wetness field consists of two layers (0–10 and 10–200 cm) measured from the surface and is given as a volumetric fraction. Equivalent water mass load is then calculated by integrating the water content in the two layers, and the inferred site displacements

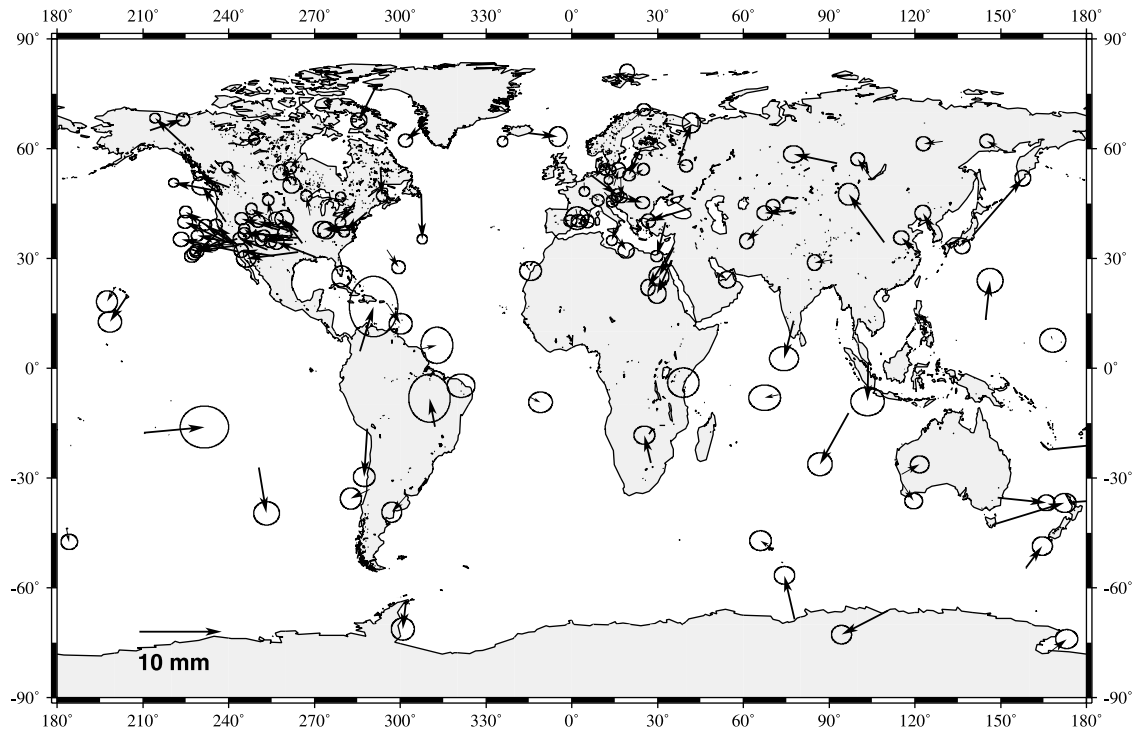


Figure 4. Vertical annual terms after atmosphere, nontidal ocean, snow, and soil wetness corrections. The amplitude and phase are defined the same way as in Figure 2.

were calculated using Green's function approach. The largest soil moisture reaches 85 cm. Annual vertical amplitudes caused by soil wetness reach 7.1, 5.3, and 5.3 mm at sites BRAZ, NSSP, and QUIN located in the center of South America, center of Eurasia, and the west coast of North America, respectively. At most continental sites, annual vertical amplitudes are $\sim 2-3$ mm. However, the grid of this simulation model seems too sparse for our study, so that the soil moisture grid values at many islands, such as Hawaii, Tahiti, and Guam, are always set to 0. As a result, the soil moisture caused seasonal coordinate variations at these islands sites are small (at submillimeter level) and are probably underestimated. Besides, the changes in subsoil water storage and vegetation are not included in our analysis for lack of quantitative model, which might be an important missing geophysical contributor to the seasonal site position variations.

[18] There is no soil moisture over Antarctica since water mass is fully represented by the snow cover. The snow cover of this model is given as the water equivalent depth (WEASD) and hence can be used directly as the mass load variation. However, there is a limitation to this model since the permanent ice fields are initially set to a large number so that the ice fields do not disappear in running the model. Thus the WEASD is defined everywhere. Over water it may have nonzero values over sea ice. A number of areas over Antarctica and Greenland possess a value of WEASD >9 m. In our computation with Green's function approach these grids were ignored. Until now the reanalysis solutions only reach December 1999. We use the snow cover and soil moisture fields from 1996 to December 1999 to adjust the seasonal parameters. The snow caused annual amplitudes of the vertical coordinates to reach 3–5 mm at high latitudes and polar regions, but only at the submillimeter level or less at low-latitude and equatorial regions, which reflects the propagated effects of the snow loading at high-latitude regions through global convection.

[19] Figure 4 shows the vertical annual terms after all the mass loading corrections have been applied, reducing the weighted mean amplitude of the annual vertical time series from 4.19 mm to 3.19 mm. At 90 out of 128 sites the vertical annual amplitudes are

reduced. Comparing Figure 4 with Figure 3, significant amplitude reduction is shown for the sites at all continents except Antarctica. The amplitudes at island sites are, on average, at the same level. Figure 5 shows the individual contributions due to nontidal ocean loading (red arrows), snow loading (green arrows), soil moisture loading (blue arrows), and atmospheric mass loading (purple arrows).

4. Searching for Potential Missing Contributors

[20] The contributions from the above known mass loading sources explain a considerable portion of the observed seasonal variations in the site coordinate time series. The residuals (Figure 4) still show systematic seasonal effects. Understanding the remaining seasonal effects will provide improved insight into the nature of the observed seasonal "deformation" as well as systematic errors resulting from the GPS data analysis itself. However, such a task is complicated because the missing sources are either highly correlated with other parameters (and hence cannot be separated directly from the data analysis), or there is no clear analytical expression relating the missing sources to the observations. Among many candidates for remaining seasonal effects, here we pick a few examples.

4.1. Atmospheric Modeling

[21] The GPS signals traverse the troposphere before reaching the receiver. Current atmospheric modeling used in GPS primary data analysis includes the following aspects. Multiple zenith delay parameters at each site spanning from 5 min to 3 hours are estimated to account for the temporary variations of troposphere. Troposphere gradient parameters are introduced [Chen and Herring, 1997; Bar-Sever et al., 1998] to reflect the spatial inclination and azimuthal heterogeneity of tropospheric layers. Niell's [1996] mapping function is adopted to characterize the seasonal difference of troposphere structure. Any mismodeling of the propagating medium effects will influence the estimates of site

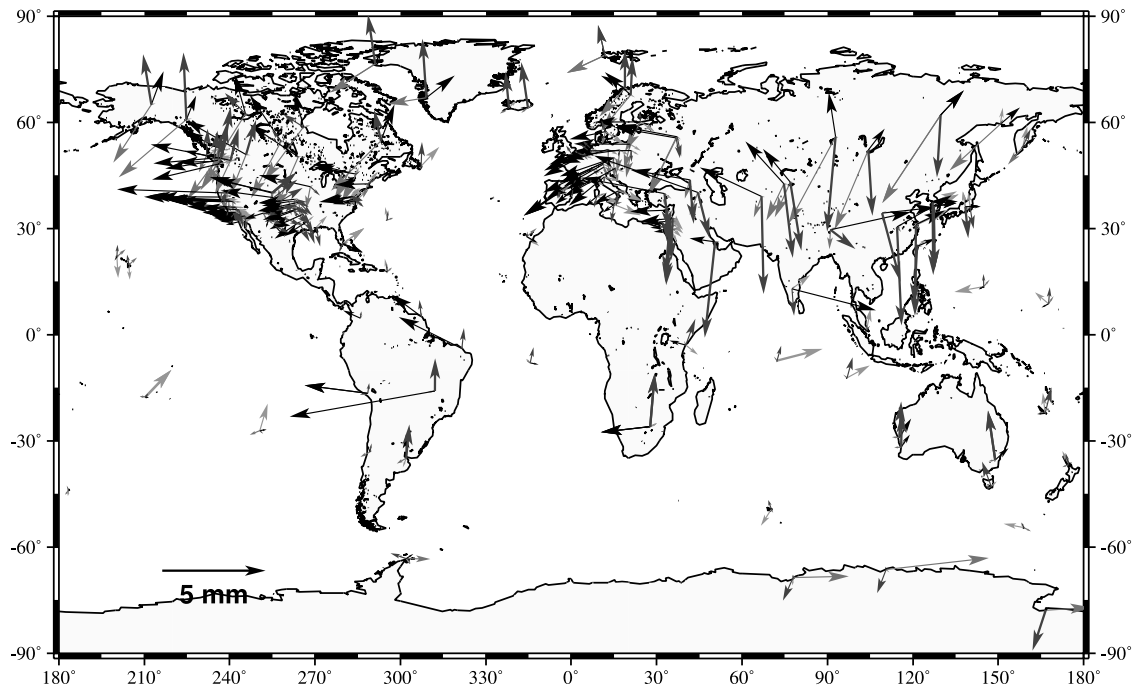


Figure 5. Atmosphere (purple arrow), nontidal ocean (red arrow), snow (green arrow), and soil wetness (blue arrow) caused vertical annual variations of site coordinates. The amplitude and phase are defined the same way as in Figure 2. See color version of this figure at back of this issue.

positions. For example, current analysis estimates total zenith delay parameters using the mapping function of hydrostatic troposphere. The wet zenith delay is not explicitly estimated because it is highly correlated with the hydrostatic zenith delay due to similar mapping functions. At low elevation angles ($<15^\circ$), the difference between the mapping functions of hydrostatic and wet atmosphere becomes noticeable. Such an approximation leaks some wet troposphere component, which is the primary seasonal component of the troposphere. How much wet zenith delay is not absorbed by the estimated total zenith delay parameters? How much wet troposphere residual enters the site position estimates? In GPS and other geodetic data analysis, such a case of highly correlated parameters is very common, and a novel and general approach should be developed to resolve the problem. Here we introduce a scaled sensitivity matrix approach (Appendix A) to answer these questions quantitatively. This approach requires GPS primary data analysis software to generate a normal consider matrix in which the contributions from both dry troposphere and wet troposphere are expressed explicitly. Then the scaled sensitivity matrix (A7) is used to assess the impact of wet zenith delay on site coordinate estimates. In this case the parameters of dry troposphere and site coordinates will be X_1 , and the parameters of wet troposphere will be X_3 . Unfortunately, the current GAMIT software does not have the function to output a complete normal consider matrix. We are unable to perform the scaled sensitivity matrix analysis in this paper.

4.2. Bedrock Thermal Expansion

[22] Bedrock thermal expansion is another potential contributor to the observed seasonal variations of site positions, primarily, to vertical positions. In Appendix B we present a simple model to estimate the contribution range from bedrock thermal expansion. Based on this half-space heat conduction model the amplitude of annual vertical variation is 0.5 mm or less. The phase of annual variation is 45° behind the phase of local annual temperature variation, i.e., at the midlatitude regions $\sim 210^\circ$ in the Northern Hemisphere, $\sim 30^\circ$ in the Southern Hemisphere (sine convention,

assuming the peak temperature, occurs on 15 July and 15 January for the Northern and Southern Hemispheres, respectively).

4.3. Phase Center Modeling and Environment Influences

[23] Phase center modeling error and local multipath also may cause apparent seasonal variations of site positions. Ground tests have shown strong coupling between phase center modeling, estimation of troposphere parameters, estimation of vertical coordinates, and the environment [Bock *et al.*, 2000], including the types of radome and pillar [Meertens *et al.*, 1996; Hatanaka *et al.*, 2001]. An interesting finding is that the phase center modeling error will enlarge the apparent seasonal amplitudes of the estimated site coordinates to the level of a few millimeters [Hatanaka *et al.*, 2001]. The mechanism of such a relation is an open question. Another open question is whether the current time-independent phase center model and local multipath model should include a seasonal factor owing to the interaction between antenna and environment. An example of environmental influence on the estimation of site position is shown in the position time series of site HOLP (Figure 1). HOLP is one of the SCIGN network sites in southern California, established [Bock *et al.*, 1995]. There was a tree of ~ 10 m high and ~ 15 m to the GPS antenna (N. King, personal communication, 2001). On 23 January 1998 the tree was trimmed to less than half its height, the estimated vertical coordinate was reduced by a 37-mm jump, and the variation pattern also changed. Such environmentally related variations are, in general, site-specific, which, though important, are beyond the scope of this paper. Seasonal antenna phase center variations caused by thermal noise were proposed [Gross and Larson, 1998], but the quantitative model has not yet been published.

4.4. Glacier Surge and Internal Ice Flow

[24] Glacier surge and ice flow cause crustal deformation in high-latitude regions near the sources. Though glacier surge varies not exactly sinusoidally, there is a seasonal aspect in that usually, the rapid movement of glacier occurs in special seasons, for instance, in late spring to late summer in the Alaska region [Saubert

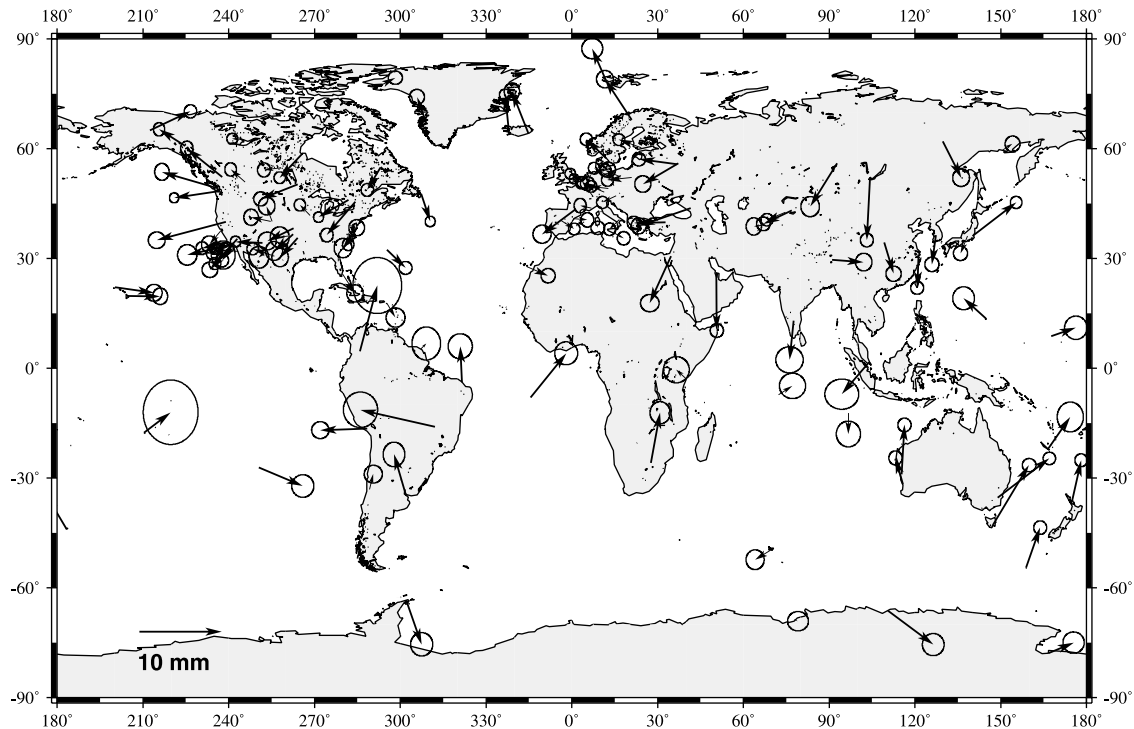


Figure 6. Vertical annual terms from Jet Propulsion Laboratory (JPL) analysis. The amplitude and phase are defined the same way as in Figure 2.

et al., 2000]. Its influence range depends on the size of ice mass change. In the case of the 1993–1995 Bering Glacier surge the influence range is within 100 km [Sauber *et al.*, 2000]. Internal ice flow occurs over a frozen or rough bed driven by internal shear, and it is close to a constant at the seasonal timescales [Wingham *et al.*, 1998], so the internal ice flow is unlikely to play significant role in the apparent seasonal deformation. Cazenave *et al.*'s [2000] estimate of the Antarctica mass balance also includes snow cover change. They report that the seasonal variations in mass balance of Antarctica may contribute to 3 mm of annual sea level fluctuation, indicating that some seasonal mass redistribution in Antarctica might be overlooked in our study.

4.5. Differences in Software and Strategies

[25] The systematic errors of processing models and software itself are important sources for the seasonal residuals. They are further divided into two categories: common errors and different errors. The second category includes the differences of analysis strategies (constraints on estimated parameters, quality control criteria, ambiguity resolution, etc.) and the software-specific errors in analysis models. Comparison between the results of different processing groups gains insight into two aspects: (1) Do all solutions detect the common seasonal signals caused by geophysical sources? (2) What are the magnitudes of seasonal systematic errors due to the second category?

4.5.1. Comparison with JPL solutions. [26] We compare our results with the daily solutions of site coordinates from the IGS process center at Jet Propulsion Laboratory (JPL) (available at <http://sideshow.jpl.nasa.gov/mbh/series.html>). The JPL solutions (from 22 January 1991 to 29 April 2000 with a total of 527 sites) were processed using the GIPSY software and the point positioning strategy [Zumberge *et al.*, 1997]. Satellite orbits were fixed to JPL precise orbits adjusted from 42 globally distributed tracking sites. For point positioning, parameters between sites are uncorrelated, so that the time series are estimated site by site. For each site the daily analysis estimates constant site position parameters, stochastic zenith delay and its gradient, white noise

stochastic receiver clock parameters, and real-value ambiguities. The JPL analysis uses a 15° elevation cutoff angle and a consistent strategy and software version. We use the JPL time series after 1996 to estimate seasonal terms through the same QOCA procedures. There are 12 sites analyzed by SOPAC that are missing in the JPL solutions or that have too short a time span to get reliable estimates of seasonal terms. Instead, we consider five nearby sites from JPL solutions with spans longer than 2 years. Figure 6 shows the resultant annual vertical terms from JPL solutions. Our reference frame defined by 36 sites is not the same as the JPL's reference frame defined by 42 tracking sites. Such a difference is small considering that both sets are globally distributed and most sites are overlapping. Since pole tide and ocean tide corrections have already been applied in the JPL primary data analysis, we impose mass loading corrections from atmosphere, nontidal ocean, snow, and soil moisture. Figure 7 shows resultant vertical annual terms after corrections. After mass loading corrections the weighted mean amplitude of the vertical annual terms is reduced from 3.49 mm to 2.89 mm. At 81 out of 121 sites the vertical annual amplitudes are reduced. Comparing Figures 3 and 6, we find very similar pattern for most sites, indicating that both SOPAC and JPL solutions are able to detect the common seasonal signals. Comparing Figure 4 with Figure 7, however, the residual annual terms are not so similar, indicating that the remaining seasonal effects are largely contaminated by different systematic errors of the two analysis centers. The JPL residuals have smaller weighted mean amplitude (2.89 versus 3.19 mm), in particular, in the North America region. One plausible explanation is that the JPL solutions are derived under a more consistent system and strategy. Three abnormal sites (FAIR, STJO, and TSKB) are identified, at which both SOPAC and JPL solutions show similar amplitude and phase (Figures 3 and 5). These solutions are inconsistent with the solutions of nearby sites and have large residuals after mass load corrections (Figures 4 and 6). They likely stem from some unmodeled local effects or instrumental troubles at the three sites. The SOPAC solution at XIAN is identified as software-dependent abnormal because (1) it

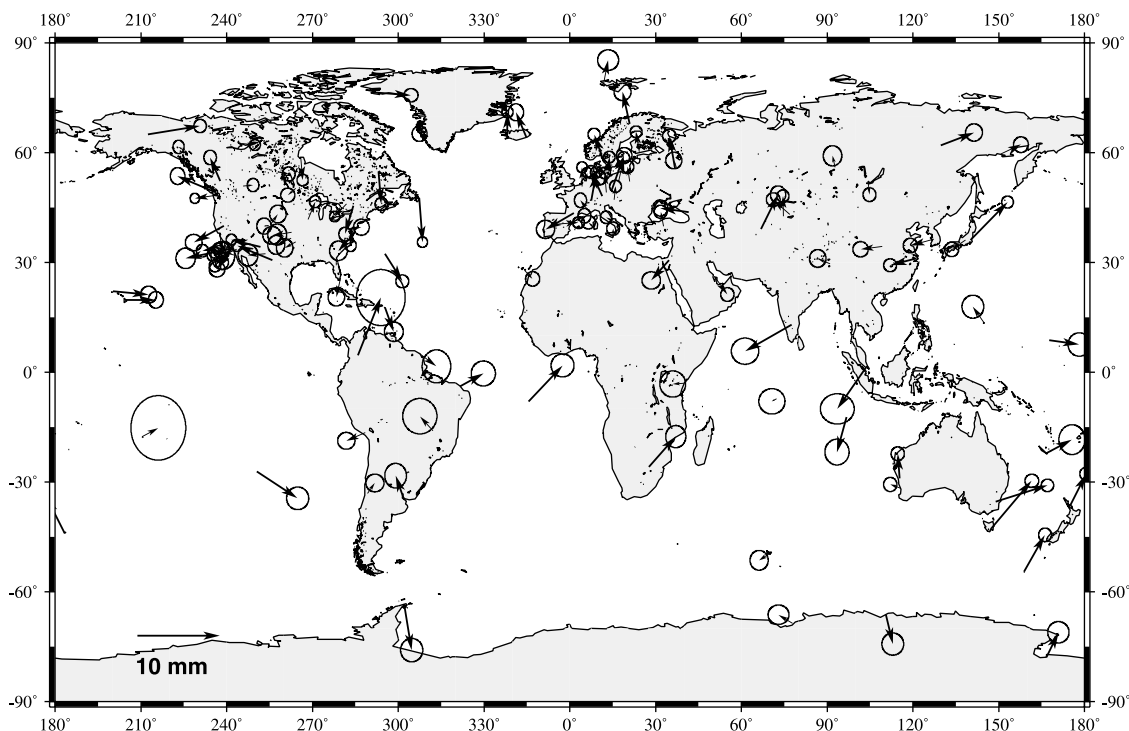


Figure 7. Vertical annual terms from JPL analysis after all mass loading corrections. The amplitude and phase are defined the same way as in Figure 2.

is out of phase with the solutions at nearby sites, and (2) it is out of phase with the mass load corrections. The possible reason is that the SOPAC XIAN solution is weak owing to the rejection of many observations during the primary data analysis. Similarly, the JPL solution at KIT3 is software-dependent abnormal. The possible reason is also similar: The JPL KIT3 time series are weak due to several gaps.

4.5.2. Comparison with GEONET solutions. [27] The GPS Earth Observation Network (GEONET) GPS array of Japan starts from 1994 with 110 sites and is augmented to 949 sites by 1996. The network is equipped with a mix of receivers (Trimble 4000SSE and 4000SSi, Ashtech Z12, and Leica SR9600). It is divided into three subnetworks on the basis of the antenna-receiver types (Trimble, Ashtech, and Leica). The Trimble subnetwork is further divided into regional clusters. Daily solutions from Trimble clusters are first combined to get Trimble subnetwork solutions through a “backbone” cluster, which consists of stations representing individual regional clusters. Then the three subnetworks data are processed independently (i.e., there are no common sites) in order to keep the antenna-receiver type homogeneous within subnetworks. Each of the Trimble, Ashtech, and Leica subnetworks has a Tsukuba stations (different benchmarks within 100 m range). Their positions have been precisely determined relative to the Tsukuba IGS station (TSKB) in the International Terrestrial Reference Frame. By tightly constraining the positions (0.1 mm) of those three Tsukuba stations to their a priori values, it is possible to obtain consistent solutions of the three uncorrelated subnetworks. The Bernese software version 4.1 [Rothacher and Mervart, 1996] is used with a 120-s decimating rate and 15° cutoff elevation angle. The IGS precise orbits and Earth rotation parameters are held fixed. Zenith total delay parameters are estimated every 3 hours, and the Hopfield troposphere mapping function is adopted. The details of network configuration and analysis strategy are documented by Miyazaki et al. [1997].

[28] We used 1170 daily solutions (from day 92, 1996, to day 218, 1999) at 787 sites (removing weak sites with formal ampli-

tude sigma >1.0 mm or phase sigma >20°) to adjust seasonal terms by the QOCA software with the same parameterization. The site displacements caused by coseismic deformation and earthquake swarms were modeled as step function parameters and were estimated simultaneously. Postseismic displacements of the 1994 Sanriku earthquake [Heki et al., 1997] and 1997 slow thrust slip induced displacements after the 1996 Hyuganada earthquake [Hirose et al., 1999] were modeled as exponential decay process

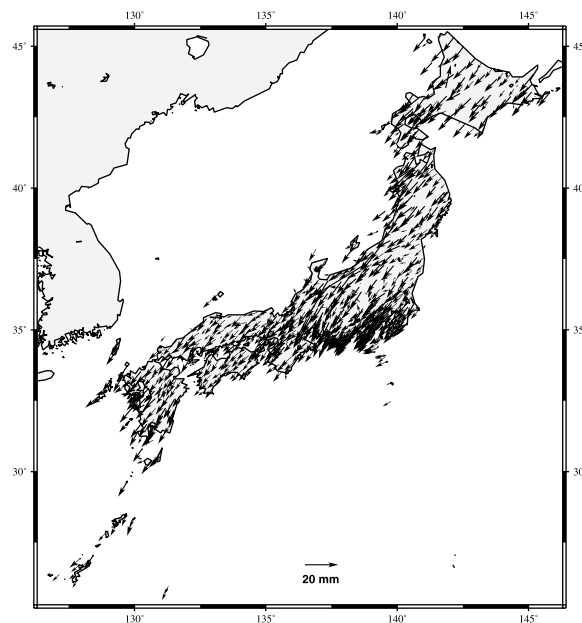


Figure 8. Vertical annual terms at GEONET sites from Geographical Survey Institute (GSI) analysis. The amplitude and phase are defined the same way as in Figure 2.

Table 2. Annual Vertical Term at USUD Relative to TSKB^a

Solution	Amplitude, mm	Phase, deg
GEONET	8.5	237.5
JPL	8.7	225.1
SOPAC	10.9	229.7

^aThe amplitude A and phase ϕ are defined as $A\sin[\omega(t-t_0) + \phi]$, where t_0 is 1996.0 and ω is the annual angular frequency. GEONET solution is the average of three local Usuda sites relative to three local Tsukuba sites.

parameters and were estimated with the other parameters simultaneously. Figure 8 plots the estimated annual vertical terms. Most sites have similar vertical annual amplitudes of ~ 5 – 10 mm with similar phase of $\sim 235^\circ$. There are a few sites that have abnormally large amplitudes due to the monument instability. Since the GEONET solutions are actually the seasonal terms relative to Tsukuba sites, we form the differential seasonal terms of SOPAC (pole tide corrected) and JPL solutions related to TSKB. There are only two sites (TSKB and USUD with Tsukuba and Usuda local sites) common in all three solutions. The comparison is listed in Table 2.

[29] Table 2 demonstrates good agreement among the three solutions. The maximum amplitude difference is <2.5 mm and maximum phase difference is $<12.5^\circ$. The agreement indicates that all three solutions are able to detect the common seasonal variation signals. The differences reflect the software-dependent errors. Since SOPAC and JPL global network analyses have identified that the observed seasonal variations at TSKB are abnormal, this implies that the nationwide annual vertical amplitudes of GEONET sites (except Tsukuba sites) are actually much smaller than 5–10 mm. The GEONET solutions further confirm that all three local Tsukuba sites (within 100 m range, different receiver types) show similar seasonal variations, indicating that the abnormal seasonal variations at Tsukuba sites are more likely caused by local environmental sources rather than instrumental problems.

4.6. Common Orbital Errors

[30] Common systematic errors in GPS analyses may be revealed by comparing the GPS results with the results from other independent techniques, such as very long baseline interferometry (VLBI). Simulation provides another approach to explore the effects of individual error sources. Investigating all potential common errors and their impacts on site coordinate estimates requires comprehensive study and is beyond the scope of this paper. Here we present one example with potential seasonal variations. All of the seasonal mass redistributions discussed in section 3 not only change the site positions geometrically, but also change Earth's gravitational field, which perturbs satellite orbits. This kind of dynamic effect is not included in current GPS routine analysis because the temporary gravity field has not yet been standardized. A typical value of the annual C_{20} amplitude caused by major surface mass redistribution is 1.01×10^{-10} [Cheng and Tapley, 1999]. Our simulations show that for a 1-month interval the maximum single epoch orbit position deviation can reach 80 cm by the end of the month from a constant 1.0×10^{-10} C_{20} perturbation. However, current routine GPS analysis mostly uses single-day (or 28 hours with 4 hours overlap) arcs to solve orbital parameters and seldom use long arcs. For a 1-day interval, such a perturbation only generates 14 mm maximum single epoch orbital position deviation and 2 mm daily mean orbital position deviation. Furthermore, such a GPS orbital deviation by C_{20} perturbation reflects changes of the orbital node rate. Such a deviation is basically absorbed by UT1 rate parameters, if we estimate network rate parameters with other parameters simultaneously. Errors in solar radiation model and transmitter phase center model have the aspect of generating seasonal variations. Although the errors in current GPS transmitter phase center model could reach meter level [Bar-Sever, 1998], most of the errors will be absorbed by other

estimated parameters (such as satellite clock parameters), similar to the case of temporary gravity field. To get a quantitative assessment of how much residual orbital error is being mapped into site coordinates, our proposed scaled sensitivity matrix approach (Appendix A) could be used.

4.7. Effects in Estimating Network Transformation Parameters

[31] Theoretically speaking, the site displacements derived from GPS analysis (after aligning to an ITRF frame) are related to a center of figure frame (CF), while the calculated site displacements from surface mass loading are related to center of solid Earth frame (CE). In the ideal case, direct comparison of the two types of site displacements will cause seasonal errors with amplitude of only 0.08 mm due to the reference frame inconsistency (Appendix C). However, in GPS analysis the CF reference frame is realized by estimating network transformation parameters (three rotations, three translations, and one scale factor) through aligning estimates site positions to a reference frame. In practice, only a limited number of core sites with less than optimal homogeneous distribution (in our case, 36 sites) can be used to define a reference frame. Thus the estimated network parameters will absorb a portion of the seasonal variations exhibited in the site positions (Appendix C). To probe this problem quantitatively, we use the mass loading predicted annual terms at the 36 core sites as ground truth to generate 2-year daily quasi-observations. The formal errors of these quasi-observations are set as 2, 2, and 5 cm for east, north, and vertical coordinates, respectively. No correlation is assigned. Then we estimate network parameters together with site positions using the same constraints as before. The results of this simple simulation indicate that the network parameters mask local annual motion amplitudes at the level of 0.4, 0.6, and 0.7 mm for east, north, and vertical coordinates, respectively.

[32] Finally, there is one question remaining: Is there real seasonal deformation from seasonal variations in fault slip and stress field? Such seasonal deformation might exist regionally, envisioned by the reports of fault slip variations induced by rainfall [Langbein *et al.*, 1990; Roeloffs, 2001]. Seasonal drainage and refill of groundwater may change the Poisson ratio of local porous bedrock, thereby producing surface displacements even under the same stress field [Peltzer *et al.*, 1998]. Such a seasonal signal, if it exists, is likely eclipsed by the seasonal variations from other sources in most regions and is not easily discernable. We leave this question for future study.

5. Discussion

[33] Observed seasonal coordinate variations record the seasonal activities of various geophysical processes, as well as the remaining seasonal systematic errors in GPS analysis. They open a door to broad GPS applications on seasonal time scales. Here we present a few examples to stimulate further investigations.

5.1. Gauge Seasonal Regional Mass Redistribution

[34] Earth is a coupled system. Seasonal mass redistribution of atmosphere, ocean, and groundwater causes relevant variations in gravity field, polar motion and UT1, geocenter, as well as variations in station coordinates. The unique contribution of the observed seasonal variations in site positions is that they directly monitor the regional seasonal mass redistribution [vanDam *et al.*, 2001]. For example, ice mass redistribution at polar and high-latitude regions plays an important role in the global climate cycle. Given that the GPS measured site positions are sensitive to ice mass transfer, they can be used with the gravity measurements to infer ice mass changes [vanDam *et al.*, 2000]. GPS observations also have been used to constrain or test glaciological ice transfer models [Sauber *et al.*, 2000]. GPS derived seasonal position terms in the high-latitude regions have the sensitivity to gauge seasonal

Table 3. Contributions of Geophysical Sources and Model Errors to the Observed Annual Vertical Variations in Site Positions

Sources	Range of Effects, mm
Pole tide	~4
Ocean tide	~0.1
Atmospheric mass	~4
Nontidal ocean mass	2–3
Snow mass	3–5
Soil moisture	2–7
Bedrock thermal expansion	~0.5
Errors in orbit, phase Center, and troposphere models	No quantitative results yet
Error in network adjustment ^a	~0.7
Differences from different software	~2–3; 5–7 at some sites

^aThe value is network-dependent.

mass variations (snow accumulation and ice sheet thinning; ice surging), if the contributions from other sources can be adequately understood.

5.2. Stabilize Reference Frame on Seasonal Timescales

[35] The ITRF is defined by a set of global tracking stations. Temporal evolution of the frame is defined by the velocities of these stations. Hence the ITRF frame maintains good long-term stability. On seasonal timescales, however, the stability of the ITRF frame suffers from unmodeled seasonal variations of the coordinates of the defining global tracking stations. It can be viewed from two aspects. First, the whole ITRF frame moves seasonally due to geocenter variations, in which the seasonal terms are primary components with amplitudes reaching 3–5 mm [Dong *et al.*, 1997; Chen *et al.*, 1999]. Second, different subsets of the ITRF global network have different relative seasonal movements. The amplitude of relative seasonal movement (estimated using both vertical and horizontal seasonal terms of the subsets) could reach 1 cm (Figure 3). Thus the seasonal solutions aligned to different subsets of ITRF tracking stations will be different. For example, the reference frame defined by site TSKB leads to 5–10 mm vertical annual amplitudes at most GEONET sites. If aligned to site USUD, the GEONET solutions will display much smaller vertical seasonal variations at most sites. Determination of the seasonal terms at global ITRF tracking stations will greatly improve the stability and accuracy of the ITRF reference frame (including its geocenter origin) on seasonal time scales. As we have shown, the seasonal geocenter variations estimated from limited tracking sites could have error of 0.6 mm, more than 10% of the seasonal geocenter amplitude. Recently Blewitt *et al.* [2000] proposed that the seasonal variation of the Earth's shape might affect the determination of the ITRF NNR frame.

5.3. Improve Assessment of GPS Error Spectrum

[36] It has been known that the long-term accuracy of GPS measurements is poorer than the short-term accuracy [Davis *et al.*, 1989; Larson and Agnew, 1991]. In the frequency domain, such a relation indicates that GPS error spectrum is not flat (white noise) and that its power spectrum is higher at low frequency. Several studies explored the nature of GPS error spectrum [King *et al.*, 1995; Johnson and Agnew, 1995; Zhang *et al.*, 1997; Mao *et al.*, 1999] using a variety of different error models. The seasonal variations of the coordinate solutions were not specifically treated though Zhang *et al.* [1997] partly removed seasonal variations common in a regional network through data stacking. As we have shown, the seasonal variations in site positions consist of signals from various geophysical sources and systematic modeling errors. Such seasonal variations should be eliminated from the time series in order to obtain more realistic assessment of the error spectrum. This might partly reconcile the discrepancy between long-term and short-term accuracy. At the current stage, such an improvement is probably minor because the dominant vertical error sources of GPS

data are instrumental and environmental. Such a situation will be changed when the instrumental noise for vertical coordinates approaches the 10 mm or lower level.

5.4. Provide Seasonal Ground Truth for GPS Analysis and Geophysical Simulation Models

[37] As the accuracy of GPS orbits and site coordinates improves, ground truth provides an important gauge to calibrate the analysis model. Short-length baseline and zero-length baseline field tests do not supply ground truth for seasonal terms because the seasonal variations at both ends of the baseline are canceled out. At the seasonal bands the contributions from known geophysical sources can serve as ground truth to provide a reasonable gauge. As a first-degree approximation, the seasonal variations of the resultant time series at GPS sites should match the patterns inferred from known geophysical processes. However, if the GPS solutions and geophysical observations reach the accuracy level of 1 mm for vertical annual amplitude, the residual seasonal terms can provide seasonal ground truth to verify the groundwater simulation models.

5.5. Potential Applications for InSAR

[38] The combination of Interferometric Synthetic Aperture Radar (InSAR) and GPS measurements provides an effective means to image the surface displacement field [Bock and Williams, 1997]. InSAR supplies unprecedented spatial resolution of a few tens of meters [Massonnet and Feigl, 1998], while GPS provides higher temporal resolution and accurate point positions for calibration. Since none of the current SAR missions were specifically designed for interferometric applications, only limited interferometric pairs can be formed. These pairs likely fall into different seasons, making seasonal displacement corrections necessary. For small areas the long-wavelength seasonal variations are not significant because the interferometric fringes are only sensitive to regional relative variations. In this case the seasonal corrections are mostly from the seasonal undulations of the local aquifer table. As InSAR applications cover larger areas, e.g., for secular and postseismic deformation studies [Peltzer *et al.*, 1998], long-wavelength seasonal variations should also be considered. Otherwise, errors on the order of several millimeters could significantly bias the solution and interpretation.

5.6. The Peering Approach

[39] Finally, we discuss the methodology used in the study of seasonal variations. The observed apparent seasonal variations of site positions include contributions from various geophysical processes, as well as from errors in modeling seasonal effects. There is no single dominant contributor (Figure 5 and Table 3). It is

Table 4. Mean Annual Vertical Amplitude and Power Explained^a

	SOPAC, mm	JPL
Mean amplitude without pole tide correction	5.47 (5.49) mm	–
Mean amplitude after pole tide correction	4.19 (4.19) mm	3.49 (3.44) mm
Mean amplitude after mass loading correction	3.19 (3.08) mm	2.89 (2.74) mm
Ratio of site numbers ^b	90/128 (90/123)	81/121 (79/116)
Power explained (pole tide and mass loading together) ^c	66% (67%)	–
Power explained (mass loading only) ^c	42% (46%)	31% (37%)

^aThe values in parentheses represent the results without five abnormal sites (FAIR, STJO, TSKB, MDVO, and XIAN for SOPAC, and FAIR, STJO, TSKB, ZWEN, and KIT3 for JPL).

^bThe numerator is the site number with reduced annual amplitudes after mass loading correction. The denominator is the total site number.

^cPower explained is defined as $1 - (A_2/A_1)^2$, where A_1 is the mean amplitude before correction and A_2 is the mean amplitude after correction.

difficult to obtain a clear picture of the observed seasonal variations by analyzing the contribution from just a single source. In the peering approach outlined in Appendix A the contributions from relatively well-known sources, such as atmospheric pressure, altimeter-measured sea-level variations, snow and soil moisture measurements, or simulated effects can be isolated. Then the contributions from more deeply hidden sources, such as potential seasonal phase center modeling errors, can be investigated. The choice of reference frame is an important consideration. It is natural to use a global reference frame in these studies. In regional reference frames, only the (much smaller) differential seasonal variations relative to tightly constrained regional tracking sites remain in the GPS time series. However, if we do not want the seasonal variations of site positions to blur the position solutions (e.g., for regional crustal motion studies), a regional reference frame may be preferred.

6. Conclusions

[40] This paper explores the nature of the observed seasonal variations in position at global GPS sites. Our investigations are summarized in Tables 3 and 4. These results demonstrate that global continuous GPS array observations are able to detect seasonal signals, as indicated by the similar patterns in the time series generated at the SOPAC and JPL analysis centers (Figures 3 and 6). These patterns are consistent with seasonal variations in site positions inferred from known geophysical sources (Figure 5). Joint contributions from surface mass redistribution (atmosphere, ocean, snow, and soil moisture) are the primary causes for the observed annual vertical variations of site positions. Pole tide and mass loading together can explain 66% of the observed power (square of mean amplitude). After pole tide correction the mass loading can explain 42% of the remaining power.

[41] We further investigate the nature of the remaining seasonal residuals after applying pole tide and mass loading corrections. Systematic differences between the solutions of different processing centers turn out to be a major cause for the residuals. Quantitatively evaluating the effects of various systematic errors and other geophysical processes is a big challenge, in particular, since many considered parameters are highly correlated. A scaled sensitivity matrix approach is proposed to quantitatively assess the contributions of highly correlated parameters (hence difficult to be estimated directly by GPS observations) such as wet troposphere component and seasonal gravity field. The issues of the ITRF frame stability on seasonal timescale and the peering approach are addressed. This paper discusses the biggest signals, i.e., the annual vertical terms, in site position time series. However, the principals and methodology are also suitable for studying semiannual vertical terms, as well as seasonal variations in the horizontal components.

[42] A recent publication by *vanDam et al.* [2001] confirms that global GPS solutions have the sensitivity to monitor seasonal surface mass distribution changes. However, there are several problems that still need to be addressed in order to better understand the nature of seasonal effects. Systematic errors in current analysis, reflected by the solution differences from different analysis centers, need to be resolved. Errors exist in the atmosphere, ocean, snow, and soil moisture data. The spatial resolution of snow and soil moisture data is not high enough to reflect local short wavelength variations. Finally, the geophysical contributors discussed in this paper are far from exclusive.

Appendix A: A Quantitative Approach for Assessing the Influences of Unresolved Parameters

[43] Assuming that the complete observation equations are

$$y = A_1X_1 + A_2X_2 + A_3X_3 + \varepsilon, \quad (A1)$$

where X_3 are the parameters, which cannot be resolved by the observations y due to high correlation with other parameters or poor sensitivity of y . X_1 are the parameters, which will be explicitly discussed, X_2 are other parameters, and ε are the observation noises. The corresponding normal matrix will be

$$\begin{bmatrix} N_{11} & N_{12} & N_{13} \\ N_{21} & N_{22} & N_{23} \\ N_{31} & N_{32} & N_{33} \end{bmatrix} \begin{bmatrix} X_1 \\ X_2 \\ X_3 \end{bmatrix} = \begin{bmatrix} u_1 \\ u_2 \\ u_3 \end{bmatrix}, \quad (A2)$$

where the normal matrix of (A2) is called the normal consider matrix

$$N_{ij} = A_i^T W A_j \quad u_i = A_i^T W y, \quad (A3)$$

and W is the observation weight matrix. The suffix T denotes transpose. Since X_3 cannot be resolved from the data, we actually solve the following normal equation

$$\begin{bmatrix} N_{11} & N_{12} \\ N_{21} & N_{22} \end{bmatrix} \begin{bmatrix} X_1 \\ X_2 \end{bmatrix} = \begin{bmatrix} u_1 \\ u_2 \end{bmatrix}. \quad (A4)$$

The least squares solution of X_1 can be written as

$$\hat{X}_1 = (N_{11} - N_{12}N_{22}^{-1}N_{21})^{-1}(u_1 - N_{12}N_{22}^{-1}u_2). \quad (A5)$$

Replacing u_1 and u_2 in (A5) by (A2), we obtain

$$\hat{X}_1 = X_1 + (N_{11} - N_{12}N_{22}^{-1}N_{21})^{-1}(N_{13} - N_{12}N_{22}^{-1}N_{23})X_3. \quad (A6)$$

Formula (A6) indicates that the estimated values of X_3 are actually the linear combinations of X_1 and X_3 . The combination coefficients are the elements of the scaled sensitivity matrix

$$(N_{11} - N_{12}N_{22}^{-1}N_{21})^{-1}(N_{13} - N_{12}N_{22}^{-1}N_{23}). \quad (A7)$$

Historically, X_3 cannot usually be measured directly, so that X_3 are treated as the stochastic variables. Formula (A6) is used to perform the consider covariance matrix analysis to provide a more realistic covariance matrix of the estimated parameters X_1 . In this case the statistical expectation of X_3 is assumed to be 0. Nowadays, however, many X_3 become measurable and can be obtained from external information. In this case, X_3 are treated as the deterministic variables, and the application of (A6) is extended to provide a quantitative gauge of the estimated X_1 . For example, the temporary gravity field zonal coefficients (C_{20} , C_{40} , C_{60} , etc.) from global atmospheric surface pressure field of the weather forecast centers were used to form the linear combination through (A6) to compare with the single satellite derived solution \hat{c}_{20} [Dong et al., 1996].

[44] If the primary GPS data analysis software can establish the complete observation (A1) and output the complete normal (A2), the same least squares solution is obtained by solving the sub-normal equation of (A2), i.e., (A4). Meanwhile, the preserved cross-correlation part of the normal matrix N_{13} and N_{23} can form the scaled sensitivity matrix (A7) to perform the rigorous correction or comparison (assuming X_3 can be derived from external sources). For example, the local integrated wet zenith delay is derived from the total zenith delay estimate [Bevis et al., 1992] by removing the hydrostatic zenith delay from the estimated total zenith delay. If the wet zenith delay is absorbed completely by the estimated zenith delay parameter, the scaled sensitivity submatrix (zenith delay part) (A7) will be an identity matrix. Thus the departure of (A7) from an identity matrix indicates that the wet zenith delay is not completely absorbed by the estimate zenith delay parameters. In general, the integrated wet zenith delays (X_3)

induced site position changes ($x_1 - \hat{x}_1$) can be accurately determined. First, the integrated wet zenith delays (X_3) are obtained either from current estimate procedures or from external resources. Then the site position part of (A6) can be used to quantitatively assess the influence of the wet troposphere components on site positions.

Appendix B: Thermal Expansion-Induced Vertical Deformation

[45] We consider a simple model. The crust is approximated as a semi-infinite half-space ($y \geq 0$) with the surface at $y = 0$ plane. The one-dimensional heat conduction equation gives

$$\frac{\partial T}{\partial y} = \kappa \frac{\partial^2 T}{\partial y^2}, \quad (\text{B1})$$

where T is the temperature and κ is the thermal diffusivity. The boundary conditions are

$$\text{at } y = 0 \quad T = T_0 + \Delta T \cos \omega t \quad (\text{B2})$$

$$\text{at } y \rightarrow \infty \quad T \rightarrow T_0, \quad (\text{B3})$$

where ω is the circular frequency of the periodic surface temperature variation and t is the time. For the annual variations, taking $\kappa = 1 \text{ mm}^2 \text{ s}^{-1}$, we get the skin depth of $\sqrt{\frac{2\kappa}{\omega}} = 3.2 \text{ m}$. Using the method of separation of variables, the solution of (B1) under boundary conditions (B2) and (B3) is

$$T = T_0 + \Delta T \exp\left(-y\sqrt{\frac{\omega}{2\kappa}}\right) \cos\left(\omega t - \sqrt{\frac{\omega}{2\kappa}}y\right). \quad (\text{B4})$$

[Turcotte and Schubert, 1982]. Taking the thermal stress into account, the total strain is

$$\begin{aligned} \varepsilon_1 &= \frac{1}{E}(\sigma_1 - \gamma\sigma_2 - \gamma\sigma_3) - \alpha_1 T \\ \varepsilon_2 &= \frac{1}{E}(-\gamma\sigma_1 + \sigma_2 - \gamma\sigma_3) - \alpha_1 T \\ \varepsilon_3 &= \frac{1}{E}(-\gamma\sigma_1 - \gamma\sigma_2 + \sigma_3) - \alpha_1 T, \end{aligned} \quad (\text{B5})$$

where γ is the Poisson's ratio, α_1 is the coefficient of linear expansion, and E is Young's modulus. Assuming that temperature T_0 is related to zero thermal stress state, the half-space is a uniform elastic medium and it is confined in horizontal directions:

$$\varepsilon_1 = \varepsilon_2 = 0; \sigma_3 = 0. \quad (\text{B6})$$

The vertical strain becomes

$$\varepsilon_3 = -\frac{1+\gamma}{1-\gamma} \alpha_1 \Delta T \exp\left(-y\sqrt{\frac{\omega}{2\kappa}}\right) \cos\left(\omega t - y\sqrt{\frac{\omega}{2\kappa}}\right). \quad (\text{B7})$$

By integrating (B7), the vertical variation at the surface is derived:

$$\Delta h = \frac{1+\gamma}{1-\gamma} \alpha_1 \Delta T \sqrt{\frac{\kappa}{\omega}} \cos\left(\omega t - \frac{\pi}{4}\right). \quad (\text{B8})$$

[46] Taking $\alpha_1 = 10^{-5}$, $\Delta T = 20^\circ$, $\gamma = 0.25$ and $\kappa = 1 \text{ mm}^2 \text{ s}^{-1}$, the amplitude of the annual surface height variation is $\sim 0.56 \text{ mm}$.

Formula (B8) indicates that for the annual cycle the surface height variation has a 1.5 month delay following the surface temperature variation. When the surface topography is significant, however, the coupling between the thermal boundary layer and the surface topography will enlarge the thermoelastic strain considerably [Harrison and Herbst, 1977].

Appendix C: Reference Frames of GPS Solutions and Mass Load Solutions

[47] Theoretically speaking, the site position solutions from GPS data analysis and the surface mass redistribution inferred site displacement solutions (Green's function approach) are with respect to different reference frames. We need to quantify what is the effect of reference frame inconsistency. There are at least three origins related to Earth-related frames [Dong et al., 1997]: the center of mass of the whole Earth including surface mass layers (CM), the center of mass of the solid Earth without load (CE), and the center of figure of the solid Earth's outer surface (CF). The Green's functions and related mass load Love numbers are defined with respect to the CE frame [Farrell, 1972], and therefore the site displacement solutions inferred from surface mass load are actually defined with respect to this frame. However, the commonly used Earth body-fixed reference frame (ITRF frame) is defined and maintained by a set of tracking sites with well-determined coordinates and velocities.

[48] The network-free GPS solutions (assuming no systematic errors) are related to the CM frame because the satellite dynamics are only sensitive to CM. While the GPS solutions are aligned to an ITRF frame by assigning network constraints or fixing fiducial stations, the origin of the frame is shifted to the origin defined by these constrained tracking sites. If the motions at these tracking sites are modeled by both secular motions and nonlinear time-dependent common geocenter motion (CF to CM), the origin of the ITRF frame will be CM. If the motions at these tracking sites are modeled only by secular motions (current case), the origin of the ITRF frame is a representation of CF. The difference between CE frame and CF frame is $\sim 2\%$ of the observed geocenter movements [Dong et al., 1997]. Here the geocenter movement is defined as the CF origin motion relative to CM frame. For 4-mm amplitude of seasonal geocenter variation the difference between CF and CE frames implies only $\sim 0.08 \text{ mm}$ amplitude seasonal error.

[49] Rigorously speaking, the values of the CF origin in the CE frame should be subtracted from the geophysical model inferred displacements at each site, then the resultant site displacements are related to CF frame and can be directly compared with the GPS solutions. In practice, the 0.08-mm amplitude seasonal error is considered small, so that we usually ignore the difference between CE and CF. In an ideal case, where the network has infinitely dense and uniformly distributed tracking sites, such a representation of CF reaches theoretically defined CF. However, if the network core sites (used to define the reference frame) have a limited number and are not globally uniformly distributed, as shown in section 4.7, the difference between CF and such a representation of CF could reach a submillimeter amplitude or even larger of seasonal variations.

[50] **Acknowledgments.** We are grateful to Tonie vanDam for providing her program for our programming, to Mike Heflin for providing time series of JPL global analysis for our comparison, and to Jeanne Sauber, Yuki Hatanaka, Ken Hurst, and Don Argus for helpful discussion. We thank Anny Cazenave, John Wahr, and an associate editor for their careful reviews and helpful suggestions. The maps in this paper were generated using the public domain Generic Mapping Tools (GMT) software [Wessel and Smith, 1995]. Our estimates of vertical annual motion at global GPS sites are available on the Web at <http://gipsy.jpl.nasa.gov/qoca> (click

“products” tag). The research described in this paper was supported under a contract with NASA at Jet Propulsion Laboratory, California Institute of Technology and NOAA grant NA77RJ0453 at Scripps Institute of Oceanography.

References

- Bar-Sever, Y. E., Estimation of GPS transmitter antenna phase center offset, *Eos Trans. AGU*, 79(45), Fall Meet. Suppl., F182, 1998.
- Bar-Sever, Y. E., P. M. Kroger, and J. A. Borjesson, Estimating horizontal gradients of tropospheric path delay with a single GPS receiver, *J. Geophys. Res.*, 103, 5019–5035, 1998.
- Beutler, G., I. I. Mueller, and R. E. Neilan, The International GPS Service for Geodynamics: Development and start of official service on January 1, 1994, *Bull. Geod.*, 68, 39–70, 1994.
- Bevis, M., S. Businger, T. A. Herring, C. Rocken, R. A. Anthes, and R. H. Ware, GPS meteorology: Remote sensing of atmospheric water vapor using the Global Positioning System, *J. Geophys. Res.*, 97, 15,787–15,801, 1992.
- Blewitt, G., Y. Bock, and G. Gendt, Regional clusters and distributed processing, paper presented at the IGS Analysis Center Workshop, Int. GPS Serv., Ottawa, Ont., 12–14 Oct., 1993.
- Blewitt, G., P. Clarke, and D. Lavallee, Spatially coherent oscillations in longitude and latitude linked to seasonal variation in Earth's shape, *Eos Trans. AGU*, 81(48), Fall Meet. Suppl., Abstract F332, 2000.
- Bock, Y., and S. Williams, Integrated satellite interferometry in southern California, *Eos Trans. AGU*, 78, 293, 299–300, 1997.
- Bock, Y., R. M. Nikolaidis, P. J. de Jonge, and M. Bevis, Instantaneous geodetic positioning at medium distances with the Global Positioning Systems, *J. Geophys. Res.*, 105, 28,223–28,253, 2000.
- Boucher, C., Z. Altamimi, and P. Sillard (Eds.), The 1997 International Terrestrial Reference Frame (ITRF97), *IERS Tech. Note 27*, Obs. de Paris, 1997.
- Cazenave, A., F. Remy, K. Dominh, and H. Douville, Global ocean mass variation, continental hydrology, and the mass balance of Antarctica ice sheet at seasonal time scale, *Geophys. Res. Lett.*, 27, 3755–3758, 2000.
- Chen, G., and T. H. Herring, Effects of atmospheric azimuthal asymmetry on the analysis of space geodetic data, *J. Geophys. Res.*, 102, 20,489–20,502, 1997.
- Chen, J. L., C. R. Wilson, R. J. Eanes, and R. S. Nerem, Geophysical interpretation of observed geocenter variations, *J. Geophys. Res.*, 104, 2683–2690, 1999.
- Cheng, M. K., and B. D. Tapley, Seasonal variations in low-degree zonal harmonics of the Earth's gravity field from satellite laser ranging observations, *J. Geophys. Res.*, 104, 2667–2682, 1999.
- Davis, J. L., W. H. Prescott, J. Svarc, and K. Wendt, Assessment of Global Positioning System measurements for studies of crustal deformation, *J. Geophys. Res.*, 94, 13,635–13,650, 1989.
- Dickman, S. R., Theoretical investigation of the oceanic inverted barometer response, *J. Geophys. Res.*, 93, 14,941–14,946, 1988.
- Dong, D., R. S. Gross, and J. O. Dickey, Seasonal variations of the Earth's gravitational field: An analysis of atmospheric pressure, ocean tidal, and surface water excitation, *Geophys. Res. Lett.*, 23, 725–728, 1996.
- Dong, D., J. O. Dickey, Y. Chao, and M. K. Cheng, Geocenter variations caused by atmosphere, ocean, and surface ground water, *Geophys. Res. Lett.*, 24, 1867–1870, 1997.
- Dong, D., T. A. Herring, and R. W. King, Estimating regional deformation from a combination of space and terrestrial geodetic data, *J. Geod.*, 72, 200–214, 1998.
- Farrell, W. E., Deformation of the Earth by surface loads, *Rev. Geophys. Space Phys.*, 10, 761–797, 1972.
- Fu, L.-L., and G. Pihos, Determining the response of sea level to atmospheric pressure forcing using TOPEX/POSEIDON data, *J. Geophys. Res.*, 99, 24,633–24,642, 1994.
- Gill, A. E., *Atmosphere-Ocean Dynamics*, Academic, San Diego, Calif., 1982.
- Gross, S., and K. Larson, Annual signals in continuous GPS time series, *Eos Trans. AGU*, 79(45), Fall Meet. Suppl., F182, 1998.
- Harrison, J. G., and K. Herbst, Thermoelastic strain and tilts revisited, *Geophys. Res. Lett.*, 4, 535–537, 1977.
- Hatanaka, Y., M. Sawada, A. Horita, M. Kusaka, J. Johnson, and C. Rocken, Calibration of antenna-radome and monument-multipath effect of GEONET, part 2, Evaluation of the phase map by GEONET data, *Earth Planets Space*, 53, 23–30, 2001.
- Heki, K., S. Miyazaki, and H. Tsuji, Silent fault slip following an interplate thrust earthquake at the Japan Trench, *Nature*, 386, 595–598, 1997.
- Herring, T. A., GLOBK: Global Kalman filter VLBI and GPS analysis program version 4.10, Mass. Inst. of Technol., Cambridge, Mass., 2000.
- Hirose, H., K. Hirahara, F. Kimata, N. Fujii, and S. Miyazaki, A slow thrust slip event following the two 1996 Hyuganada earthquakes beneath the Bungo Channel, southwest Japan, *Geophys. Res. Lett.*, 26, 3237–3240, 1999.
- Hurst, K. J., D. A. Argus, A. Donnellan, M. B. Heflin, D. C. Jefferson, G. A. Lyzenga, J. W. Parker, M. Smith, F. H. Webb, and J. F. Zumberge, The coseismic geodetic signature of the 1999 Hector Mine Earthquake, *Geophys. Res. Lett.*, 27, 2733–2736, 2000.
- Johnson, H. O., and D. C. Agnew, Monument motion and measurements of crustal velocities, *Geophys. Res. Lett.*, 22, 2905–2908, 1995.
- Kanamitsu, M., W. Ebisuzaki, J. Woolen, J. Potter, and M. Fiorino, Overview of NCEP/DOE Reanalysis-2, paper presented at the Second International Conference on Reanalyses, World Clim. Res. Prog., Reading, UK, 23–27 Aug., 1999.
- King, N. E., J. L. Svarc, E. B. Fogleman, W. K. Gross, K. W. Clark, G. D. Hamilton, C. H. Stiffer, and J. M. Sutton, Continuous GPS observation across the Hayward fault, California, 1991–1994, *J. Geophys. Res.*, 100, 20,271–20,284, 1995.
- King, R. W., and Y. Bock, Documentation for the GAMIT GPS analysis software version 10.03, Mass. Inst. of Technol., Cambridge, Mass., 2000.
- Langbein, J. D., R. D. Burford, and L. E. Slater, Variations in fault slip and strain accumulation at Parkfield, California, *J. Geophys. Res.*, 95, 2533–2552, 1990.
- Larson, K. M., and D. C. Agnew, Application of the Global Positioning System to crustal deformation measurement, I, Precision and accuracy, *J. Geophys. Res.*, 96, 16,547–16,565, 1991.
- Levitus, S., and T. P. Boyer, *World Ocean Atlas 1994*, vol. 4, *Temperature*, 129 pp., Natl. Environ. Satell. Data and Inf. Serv., Silver Spring, Md., 1994.
- MacMillan, D. S., and C. Ma, Analysis of residual VLBI geodetic time series, *Eos Trans. AGU*, 81(48), Fall Meet. Suppl., F314, 2000.
- Mangialotti, S., A. Cazenave, L. Soudarin, and J. F. Cretaux, Annual vertical crustal motions predicted from surface mass redistribution and observed by space geodesy, *J. Geophys. Res.*, 106, 4277–4291, 2001.
- Mao, A., C. G. A. Harrison, and T. H. Dixon, Noise in GPS coordinate time series, *J. Geophys. Res.*, 104, 2797–2816, 1999.
- Massonnet, D., and K. L. Feigl, Radar interferometry and its application to changes in the Earth's surface, *Rev. Geophys.*, 36, 441–500, 1998.
- McCarthy, D. D. (Ed.), IERS Conventions 1996, *IERS Tech. Note 21*, Int. Earth Rotation Serv., Obs. de Paris, Paris, Jul. 1996.
- Mcphaden, M. J., Genesis and evolution of the 1997–1998 El Niño, *Science*, 283, 950–954, 1998.
- Meertens, C., C. Alber, J. Braun, C. Rocken, B. Stephens, R. Ware, M. Exner, and P. Kolesnikoff, Field and anechoic chamber tests of GPS antennas, paper presented at the IGS Analysis Center Workshop, Int. GPS Serv., Silver Spring, Md., Jun. 1996.
- Miyazaki, S., T. Saito, M. Sasaki, Y. Hatanaka, and Y. Iimura, Expansion of GSI's nationwide GPS array, *Bull. Geog. Surv. Inst.*, 43, 23–34, 1997.
- Niell, A. E., Global mapping functions for the atmosphere delay at radio wavelengths, *J. Geophys. Res.*, 101, 3227–3246, 1996.
- Peltzer, G., P. Rosen, F. Roges, and K. Hudnut, Poroeleastic rebound along the Landers 1992 earthquake surface rupture, *J. Geophys. Res.*, 103, 30,131–30,145, 1998.
- Roads, J., T. Reichler, S. Chen, M. Kanamitsu, and W. Ebisuzaki, Surface water characteristics and influences in NCEP/DOE Reanalysis-2, paper presented at the Second International Conference on Reanalyses, Reading, UK, 23–27 Aug., 1999.
- Roeloffs, E. A., Creep rate changes at Parkfield, California 1966–1999: Seasonal, precipitation induced, and tectonic, *J. Geophys. Res.*, 106, 16,525–16,548, 2001.
- Rothacher, M., and L. Mervart, The Bernese GPS software version 4.0, Astron. Inst., Univ. of Berne, Berne, Switzerland, 1996.
- Sauber, J., G. Pfaffner, B. F. Molnia, and M. A. Bryant, Crustal deformation associated with glacial fluctuations in the eastern Chugach Mountains, Alaska, *J. Geophys. Res.*, 105, 8055–8077, 2000.
- Scherneck, H. G., A parameterized solid Earth tide model and ocean tide loading effects for global geodetic baseline measurements, *Geophys. J. Int.*, 106, 677–694, 1991.
- Tapley, B. D., D. P. Chambers, C. K. Shum, R. J. Eanes, J. C. Ries, and R. H. Stewart, Accuracy assessment of the large-scale dynamic ocean topography from TOPEX/Poseidon altimetry, *J. Geophys. Res.*, 99, 24,605–24,618, 1994.
- Turcotte, D. L., and G. Schubert, *Application of Continuum Physics to Geological Problems*, 450 pp., John Wiley, New York, 1982.
- vanDam, T. M., and T. A. Herring, Detection of atmospheric pressure loading using very long baseline interferometry measurements, *J. Geophys. Res.*, 99, 4505–4517, 1994.
- vanDam, T. M., and J. M. Wahr, Displacements of the Earth's surface due to atmospheric loading: Effects on gravity and baseline measurements, *J. Geophys. Res.*, 92, 1281–1286, 1987.
- vanDam, T. M., G. Blewitt, and M. B. Heflin, Atmospheric pressure load-

- ing effects on Global Positioning System coordinate determinations, *J. Geophys. Res.*, *99*, 23,939–23,950, 1994.
- vanDam, T. M., K. Larson, J. M. Wahr, S. Gross, and O. Francis, Using GPS and gravity to infer ice mass change in Greenland, *Eos Trans. AGU*, *81*, 421, 426–427, 2000.
- vanDam, T. M., J. M. Wahr, P. C. D. Milly, A. B. Shmakin, G. Blewitt, D. Lavallee, and K. M. Larson, Crustal displacements due to continental water loading, *Geophys. Res. Lett.*, *28*, 651–654, 2001.
- Wessel, P., and W. H. F. Smith, New version of the Generic Mapping Tools released, *Eos Trans. AGU*, *76*, 329, 1995.
- Wingham, D. J., A. J. Ridout, R. Scharroo, R. J. Arthern, and C. K. Shum, Antarctic elevation change from 1992 to 1996, *Science*, *282*, 456–458, 1998.
- Zhang, J., Continuous GPS measurements of crustal deformation in southern California, Ph.D. dissertation, Univ. of Calif., San Diego, 1996.
- Zhang, J., Y. Bock, H. Johnson, P. Fang, S. Williams, J. Genrich, S. Wdowinski, and J. Behr, Southern California permanent GPS Geodetic Array: Error analysis of daily position estimates and site velocities, *J. Geophys. Res.*, *102*, 18,035–18,055, 1997.
- Zumberge, J., M. B. Heflin, D. C. Jefferson, M. M. Watkins, and F. H. Webb, Precise point positioning for the efficient and robust analysis of GPS data from large networks, *J. Geophys. Res.*, *102*, 5005–5017, 1997.
-
- M. K. Cheng, Center for Space Research, University of Texas at Austin, Austin, TX 78759, USA. (cheng@csr.utexas.edu)
- D. Dong, Jet Propulsion Laboratory, California Institute of Technology, 4800 Oak Grove Dr., Pasadena, CA 91109, USA. (Danan.Dong@jpl.nasa.gov)
- P. Fang and Y. Bock, Institute of Geophysics and Planetary Physics, Scripps Institution of Oceanography, La Jolla, CA 92093, USA. (pfang@pcca.ucsd.edu; ybock@ucsd.edu)
- S. Miyazaki, Earthquake Research Institute, University of Tokyo 1-1, Yayoi-1, Bunkyo-ku, Tokyo 113-0032, Japan. (miyazaki@eri.u-tokyo.ac.jp)

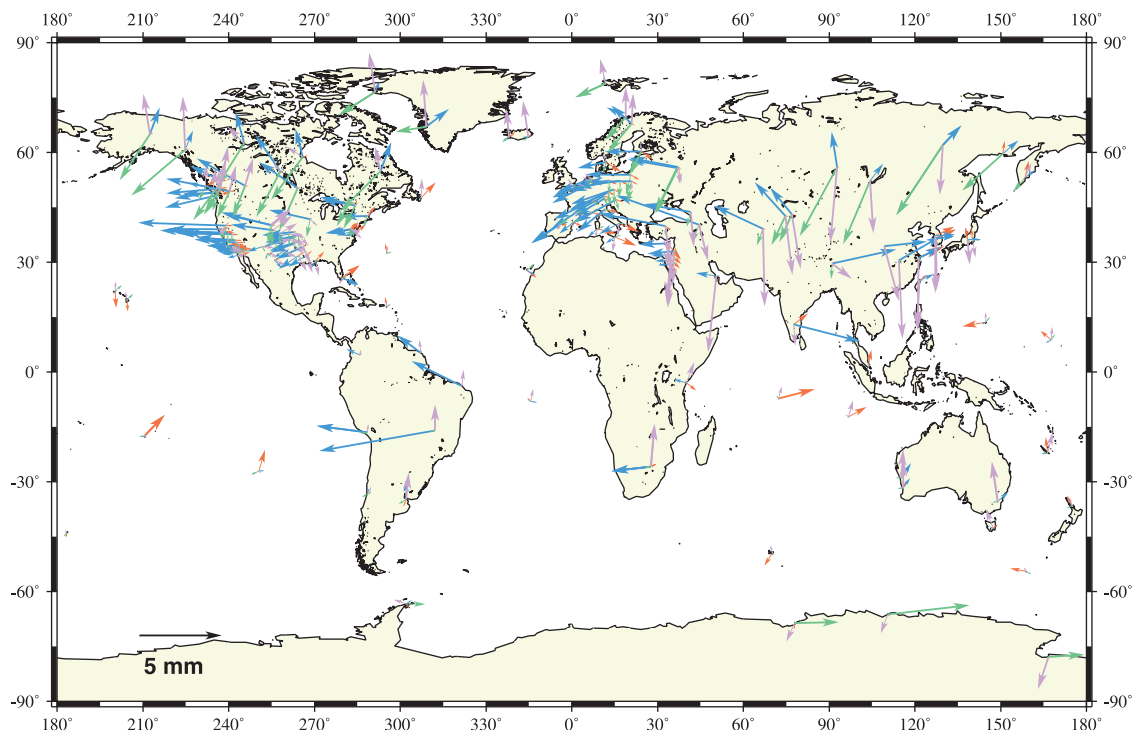


Figure 5. Atmosphere (purple arrow), nontidal ocean (red arrow), snow (green arrow), and soil wetness (blue arrow) caused vertical annual variations of site coordinates. The amplitude and phase are defined the same way as in Figure 2.